Spring 2018

EXPERIMENTAL STUDIES OF FATIGUE PERFORMANCE OF INCONEL 718 AND FIBERGLASS REINFORCED VINYLESTER

Sean Gribbin
University of New Hampshire, Durham

EXPERIMENTAL STUDIES OF FATIGUE PERFORMANCE OF INCONEL 718 AND FIBERGLASS REINFORCED VINYLESTER

BY

SEAN GRIBBIN

Bachelor of Science, Mechanical Engineering, University of New Hampshire, 2014

THESIS

Submitted to the University of New Hampshire

In Partial Fulfillment of

The Requirements for the Degree of

Master of Science

in

Mechanical Engineering

May, 2018

This thesis has been examined and approved in partial fulfillment of the requirements for the degree of Master of Science in Mechanical Engineering by:

Thesis Director, Igor I. Tsukrov
Professor of Mechanical Engineering
University of New Hampshire

Marko Knezevic
Assistant Professor of Mechanical Engineering
University of New Hampshire

Jud DeCew, Ph.D.
Director of Engineering
HALO Maritime Defense Systems

On 3/23/2018

Original approval signatures are on file with the University of New Hampshire Graduate School.

ACKNOWLEDGEMENTS

I would like to express my utmost gratitude to my mentors and peers at UNH, without whom this work would not be possible. It has been an absolute pleasure to work under the guidance and encouragement of my advisor, Professor Igor Tsukrov, along with the technical expertise of Professors Marko Knezevic, Brad Kinsey, Yannis Korkolis and Todd Gross in support. I would also like to thank Madhav Baral and Nengxiu Deng for their guidance and instruction on the use of lab equipment, Derek Smith and Saeede Ghorbanpour for their contributions to this thesis, and to all the students and professors in the Mechanics, Materials, and Manufacturing lab group for their critiques, suggestions and most importantly, their friendship. I have thoroughly enjoyed my seven years here at UNH, and I am proud to have had the opportunity to obtain my second degree here.

This work was supported by the New Hampshire Innovation Research Center, TURBOCAM International and HALO Maritime Defense Systems. I would also like to acknowledge Jonathan Bicknell and Luke Jorgensen from TURBOCAM and Dr. Judson DeCew from HALO Maritime Defense Systems for their support of my work.

TABLE OF CONTENTS

LIST OF TABLES

LIST OF FIGURES

ABSTRACT

EXPERIMENTAL STUDIES OF FATIGUE PERFORMANCE OF INCONEL 718 AND FIBERGLASS REINFORCED VINYLESTER

by

Sean Gribbin

University of New Hampshire, May, 2018

Fatigue performance of structural materials depend on their microstructure and manufacturing processes. In this thesis, two different materials are investigated: additively manufactured Inconel 718 and a fiberglass reinforced vinylester composite.

The microstructural features of a direct metal laser sintered Inconel 718 are compared to a traditionally manufactured wrought Inconel 718. The effects of 3D printing direction and heat treatment are studied. Low cycle fatigue specimens manufactured by Turbocam International are tested at strain amplitudes from 0.6% to 1.4% engineering strain. These data are correlated to the microstructural features seen in the electron backscatter diffraction. High cycle fatigue specimens are tested at stress amplitudes ranging from 200 MPa to 1200 MPa. Images of the fracture surfaces are utilized to find trends in the ductile and brittle fracture areas on the surface to understand the material performance in fatigue. Strain-life and stress-life curves are generated for the low cycle and high cycle fatigue data, respectively.

The low cycle fatigue performance of fiberglass reinforced vinylester is also investigated. Specimens manufactured by HALO Maritime Defense Systems are subjected to tension-tension fatigue loading with maximum stresses ranging from 250 MPa to 350 MPa. A stress-life curve is generated and the results are compared to data from literature. It is observed that these composite materials have high uncertainty in fatigue performance so it is recommended to use a lower bound S-N curve for design purposes.

I. INTRODUCTION

I.1. Direct metal laser sintering as a new manufacturing process for Inconel parts

Additive manufacturing (AM) of polymer materials for prototypes has a 20-year history and has been a well explored research topic [1–4]. Recently, the feasibility of using metal AM material as functional parts rather than simple prototypes or assembly testing components has been a popular focus of research. Santos et al. [1] provides a list of these studies and gives a comprehensive overview of the different systems utilized for laser-equipped rapid manufacturing machines as well as a historical perspective of the technology.

The focus of this thesis falls within a subsection of additive manufacturing known as direct metal laser fabrication (DMLF). A summary of the different classifications of DMLF is shown in Figure I.1 [5, 6].

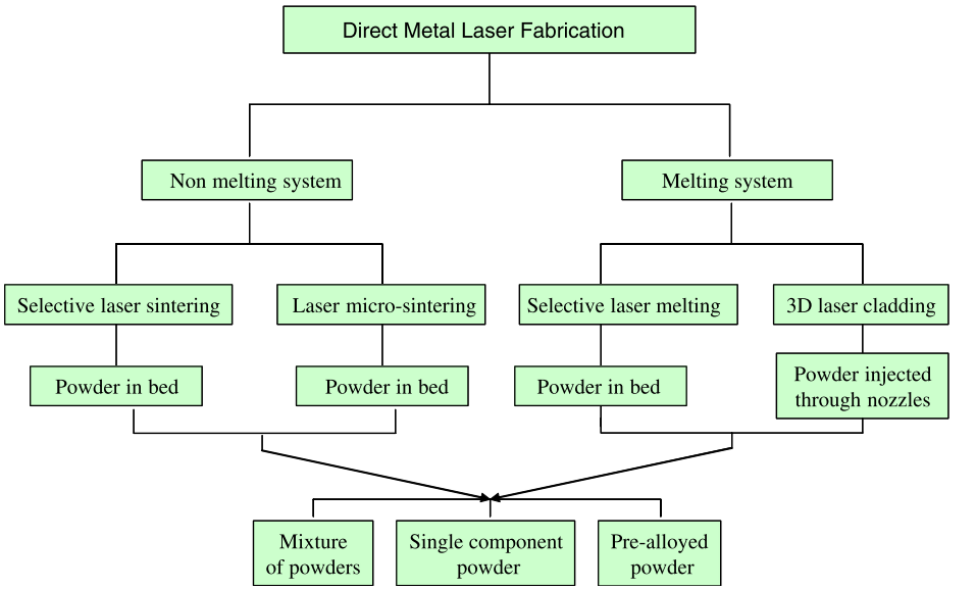

Figure I.1. Classification of rapid manufacturing techniques for direct metal laser fabrication [1].

Within DMLF, there are systems in which the metal powder is completely melted and resolidified and partial-melting techniques where the powder particles are sintered together. The powder can also be laid in a bed or injected through a nozzle to the laser melting or sintering site. Selective laser sintering (SLS), or direct metal laser sintering (DMLS) is a partial-melting, powder-in-bed type that is the AM technique of interest in this thesis.

In this process, a part is built layer-by-layer inside a sealed build chamber as shown in Figure I.2. A roller deposits a thin layer of powder onto a build surface and a guided laser then scans over the layer, sintering the particles together [1]. After the first layer is finished, the build surface drops down one-layer thickness and the process is repeated until the part is completed, while the remaining powder acts as a support for the completed part.

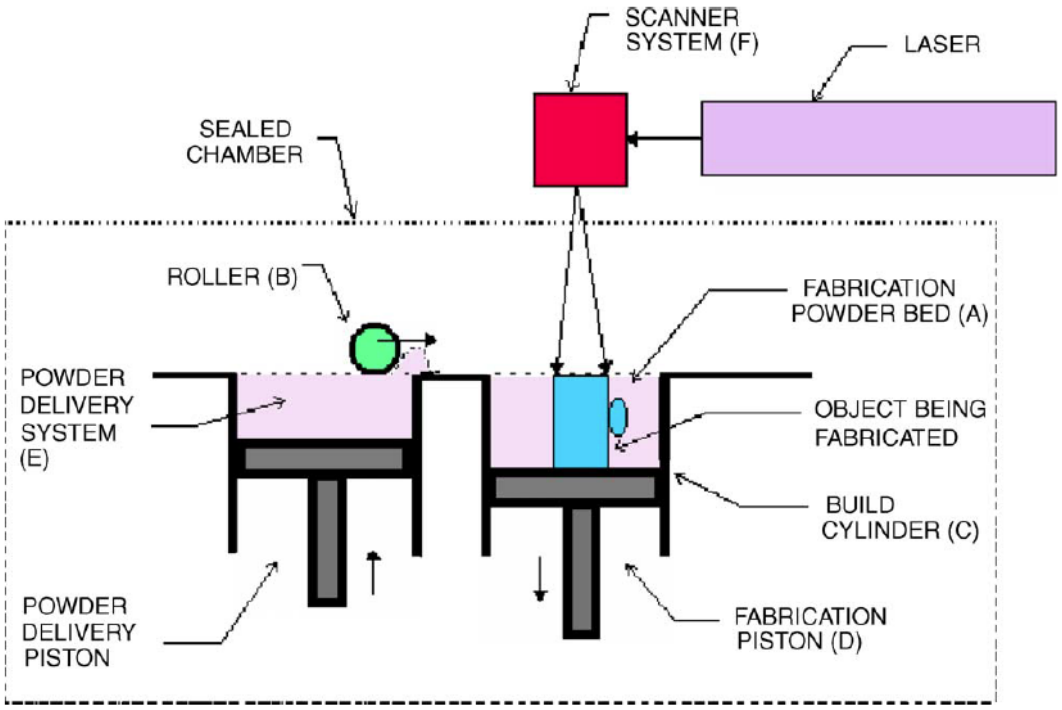

Figure I.2. Schematic of a direct metal laser sintering process [1].

The sealed chamber is filled with an inert gas to prevent oxidation of the part. Layer thicknesses typically range from 20 μm to 100 μm and depend on the powder particle sizes, which also range from <1 μm to 100 μm [1].

DMLS of aerospace alloys has been increasingly evaluated to complement production of complex shape parts [1, 7]. DMLS is a rapid manufacturing process that has the advantage of eliminating the need for extensive machining and expensive tooling over traditional manufacturing techniques such as forging [1, 7, 8].

Several studies have been performed to compare the quality of DMLS built and traditionally manufactured samples of Inconel 718, mostly focusing on the material microstructure and quasi-static properties. Zhao et al. [9] compared tensile strength, elongation, and rupture lifetime of deposited vs. wrought and cast Inconel 718 and related the differences to the base powder type and post treatment conditions. After certain heat treatment conditions, the tensile properties of printed and wrought material were comparable. However, ductility and rupture life were reduced in the deposited material compared to wrought and cast material mainly due to the presence of porosity. Amato et al. [10] performed a comprehensive study characterizing the hardness and tensile properties of DMLS built Inconel 718 as well as microstructural features in as built, heat treated and hot isostatically pressed (HIP) conditions. Liu et al. [11] investigated the relationship between two laser scanning paths and their associated heat transfer mechanisms to describe differences in microstructure formations and associated mechanical properties. The room temperature tensile strength was similar but ductility varied substantially, which was correlated with inhomogeneity in the grain structure. DMLS can introduce a highly inhomogeneous microstructure with grains elongated in the build direction [9–13]. Furthermore, DMLS materials are known to develop porosity, which is detrimental for material strength and failure behavior [14]. The development of

porosity has been attributed to a turbulent condition created by the high temperature melt pool [15]. An additional laser pass, referred to as “re-melting” usually helps reduce porosity in the DMLS built specimens [16]. However, this re-melting pass increases production time. A simultaneous heat and pressure treatment, referred to as hot isostatic pressing (HIP), can be applied to close the internal porosity [17, 18].

In Smith et al. [19] the build orientation and post-treatment processes of DMLS fabricated Inconel 718 were correlated with its microstructure and static mechanical properties. Characterization of the material by electron backscattered diffraction (EBSD) revealed elongated grain structure and formation of <001> fiber texture along the build direction (BD). The mechanical response under tension and compression was found to vary with the testing direction by approximately 7%, which was governed by a combination of grain structure and crystallographic texture. Anisotropy of the material flow during compression was observed to be significant, as well as tension-compression asymmetry in the yield stress. Treatment by HIP was found to lower yield stress but improve ductility relative to the annealed and aged material. These observations suggested that the low cycle fatigue behavior of DMLS fabricated Inconel 718 could also be dependent on the build orientation and post processing treatment of the material.

In Xiao et al. [20], the microstructure and low cycle fatigue performance of wrought Inconel 718 at room temperature were investigated relative to the concentration of Boron in the material. The strain-life fatigue curve was observed to have an inflection point at a plastic strain amplitude of 0.4%. For this reason, a bilinear Coffin-Manson relation was suggested to better describe the fatigue behavior. The effect of minor elements on properties of Ni-based superalloys has been reviewed in [21].

In Kawagoishi et al (2000), the performance of wrought Inconel 718 under rotary bending fatigue at room temperature, 300 °C, 500 °C and 600 °C was investigated using plain cylindrical specimens [22]. The initiation and growth of fatigue cracks in rotary bending fatigue was observed using notched specimens. It was found that the fatigue strength increases with the increase in temperature, except in the short-life region of the material, where room temperature material performed better than elevated temperature material. Based on observations made in the crack growth, it was deemed that in the short-life region, softening of the material with elevated temperature decreases the fatigue strength. However, in the long-life region, oxidation of crack surfaces slows crack growth, increasing the life of the material.

In this thesis, the low and high cycle fatigue performance of DMLS Inconel 718 is investigated and compared with that of the traditionally manufactured Inconel 718.

I.2. Utilization of polymers and composites in ocean engineering

The use of composite materials in marine environments dates back to shortly after World War II, when boat builders began using fiber reinforced polymer composites as a replacement for wood, as wood was becoming scarce and expensive. There was a need for a lightweight and durable material that could withstand the harsh corrosive environments of the ocean. Since then, the marine industry has demanded the expanded use of these materials, not only in ship hull design, but ship propellers, radomes, and offshore structures [23].

Numerous studies have been conducted to evaluate the performance of composite materials in normal conditions as well as the harsh environments of the ocean. In Narasihma Murphy et al. [24] the water uptake, shear strength, flexural strength, and tensile strength were measured relative to the time period of seawater aging. It was observed that epoxy based composites showed inferior

water uptake behavior to vinyl based composites. Over a one-year soaking period, the flexural strength and ultimate tensile strength (UTS) dropped by about 35% and 27% for glass/epoxy, 22% and 15% for glass/vinyl ester, 48% and 34% for carbon/epoxy 28%, and 21% carbon/vinyl ester composites respectively, showing that vinyl composites are better suited for marine environments. Observations from images taken on a scanning electron microscope showed that moisture penetration weakened the fiber/matrix interface causing interfacial debonding.

In Miller et al. [25] the effect of seawater aging at 40 °C and 50 °C on tensile and compressive properties was evaluated for a fully-saturated unidirectional laminate in the longitudinal and transverse directions. The tensile fatigue strength was also evaluated for the longitudinal direction. The tensile and compressive strength were observed to reduce with increasing moisture and temperature in the longitudinal direction, while in the transverse direction, compressive strength decreases and tensile strength is little affected as temperature and moisture increase. The fatigue strength of the conditioned samples is reduced at high stress levels, but matches the unconditioned samples at lower stress levels.

In this thesis, the low cycle fatigue of a fiberglass-vinylester composite to potentially be utilized by HALO Maritime Defense Systems, a partner in this study, is investigated.

II. INCONEL 718 SPECIMEN PREPARATION AND MICROSTRUCTURAL FEATURES

In this chapter, the specifications of the sintering process as well as the heat treatments that the Inconel 718 samples underwent are outlined. Electron backscattered diffraction (EBSD) was used to characterize microstructural characteristics of direct metal laser sintered (DMLS) Inconel 718 superalloy and compare to a traditionally manufactured wrought Inconel 718. The results presented in this chapter are to be used to supplement results and discussion with the related fatigue studies seen in Chapters III and IV. This work was published in December 2016 in *International Journal of Fatigue*, and the co-authors' contributions to this thesis are greatly appreciated [26].

II.1. Inconel 718 specimen manufacturing and heat treatment

The Inconel 718 samples discussed in Chapters III and IV were manufactured in an *EOS M280* DMLS machine using the powder produced by gas atomization with a chemical composition meeting the Inconel 718 standard. The chemical composition of the powder was (wt%) 55.5 Ni, 18.2 Cr, 5.5 Nb, 3.3 Mo, 0.35 Si, 0.35 Mn, 0.3 Cu, 1.15 Ti, 0.3 Al, 0.08 C, 0.015 P, 0.015S, 0.006 B, and balance Fe. The particle sizes ranged from <1μm to 80μm with a mean of 35μm in diameter. The power of the Yb-fibre laser varied in operation with a maximum output of 400W. Laser spot diameter at the metal pool was roughly 100 μm.

The material was sintered in 40 μm thick layers. Each layer was built by linear passes of the laser, however the direction of laser movement was rotated by 67º between the consecutive layers to avoid matching melt pool lines until multiple layers had passed. The build chamber was sealed to prevent atmospheric contaminants from entering the build. Ultra-high purity argon was purged

into the chamber and constantly flown over the build area to keep an oxygen content lower than 0.1%. The chemical stability of the material benefited from a low oxygen content as it experiences phase changes throughout the building process. To reduce the stress induced by thermal cycles, the build platform was heated to 80ºC. Thermal conduction throughout the component helped with pre-heating before sintering. The selected laser power was enough for melt pool to reach three layers at a time. This allowed for recrystallization of the deeper layers and the sintering of another. After the core of the cross section was sintered, there were two non-linear passes that followed the outside contour. These passes resulted in dimensional accuracy and surface finish of the part. However, due to the melt pool interruption between the inside and outside contours there was a known area of porosity in the external layer of the part, see [19].

The DMLS samples subsequently underwent heat treatment (HT) after which a few samples were further subjected to hot isostatic pressing (HIP). Post-processing HT is typically applied to improve properties of the DMLS parts because DMLS microstructures usually contain non-equilibrium phases as well as very high residual thermal stresses [27]. Vacuum furnace was used for heat treating a set of samples per AMS 5663 as follows. The solution HT was performed at 954 °C for 1 h, followed by fan cooling in argon to below 120 °C. Subsequently, the double aging HT was carried out, which consisted of holding at 718 °C for 8 h, followed by furnace cooling at a rate of 50 °C/h to 621 °C and holding at 621 °C for 8 h, and finally air cooled to room temperature. The HT temperatures were not sufficiently high to recrystallize or to fully stress relieve the material [28]. Subsequently, a set of samples underwent HIP at 1163 °C for 4 h under 100 MPa. The HIP temperature was high enough to trigger recrystallization. HIPing is known to entirely stress relieve the alloy microstructure [9].

To compare the low and high cycle fatigue performance of DMLS and traditionally manufactured alloys, wrought specimens were cut from shaped forgings of Inconel 718 with sample loading direction perpendicular to the original forging load direction. Since the wrought material was used for comparison with the additively manufactured material, the forgings were subjected to the same heat treatment as the DMLS material as prescribed by AMS 5663 before the samples were machined.

II.2. Microstructural features of DMLS Inconel 718

Inconel 718 is the most widely used commercial Ni based superalloy. It is a γ' and γ'' precipitate hardened alloy [29]. It contains approximately three weighted percent of γ' and nine weighted percent of γ'' [30]. Additionally, δ precipitates are also present but their fraction is minimized as much as possible to less than one weighted percent [30]. The γ' precipitate is a Ni3(Al,Ti) compound having a face-centered cubic (FCC) crystal structure [31] and a spherical geometry [29]. The diameter of the γ' precipitate is between 10 nm and 40 nm [32]. The γ'' precipitate is a body-centered tetragonal (BCT) Ni3Nb compound [31] with a disk shaped geometry [29]. The γ' and γ'' precipitates are similar in size in alloy 718. The δ precipitates have a needle-shaped geometry ranging in length between 1-8 μm [32–34]. These precipitates are generally detrimental to mechanical properties unless they form in spherical morphology at the grain boundaries, where they improve the material's creep behavior by preventing grain boundary sliding as a creep mechanism [33, 35]. In forged billets, grain structure depends on the location within the billets due to dissimilar heat transfer conditions at various locations. The grain size distribution can range between 10 μm to 100 μm in as-forged Inconel 718 [36].

Figure II.1 shows initial microstructure in the samples manufactured using (a) DMLS followed by double-aging, (b) DMLS followed by double aging and HIPing, and (c) forging followed by double-aging. The initial microstructures of the three sample categories were characterized by electron backscattered diffraction (EBSD). The individual samples were mechanically prepared using automated grinding and polishing procedures. To this end, a series of SiC papers were used to grind the specimens. After grinding, the samples were polished on a cloth using 5 µm, 0.5 µm, 0.05 µm alumina suspension. Final polishing of the samples was done with 0.02 µm colloidal silica suspension. The automated EBSD data collection was performed using the Pegasus system (Octane Plus SDD detector and Hikari High Speed Camera) attached to a Tescan Lyra (Ga) field emission scanning electron microscope (SEM) at a voltage of 20 kV.

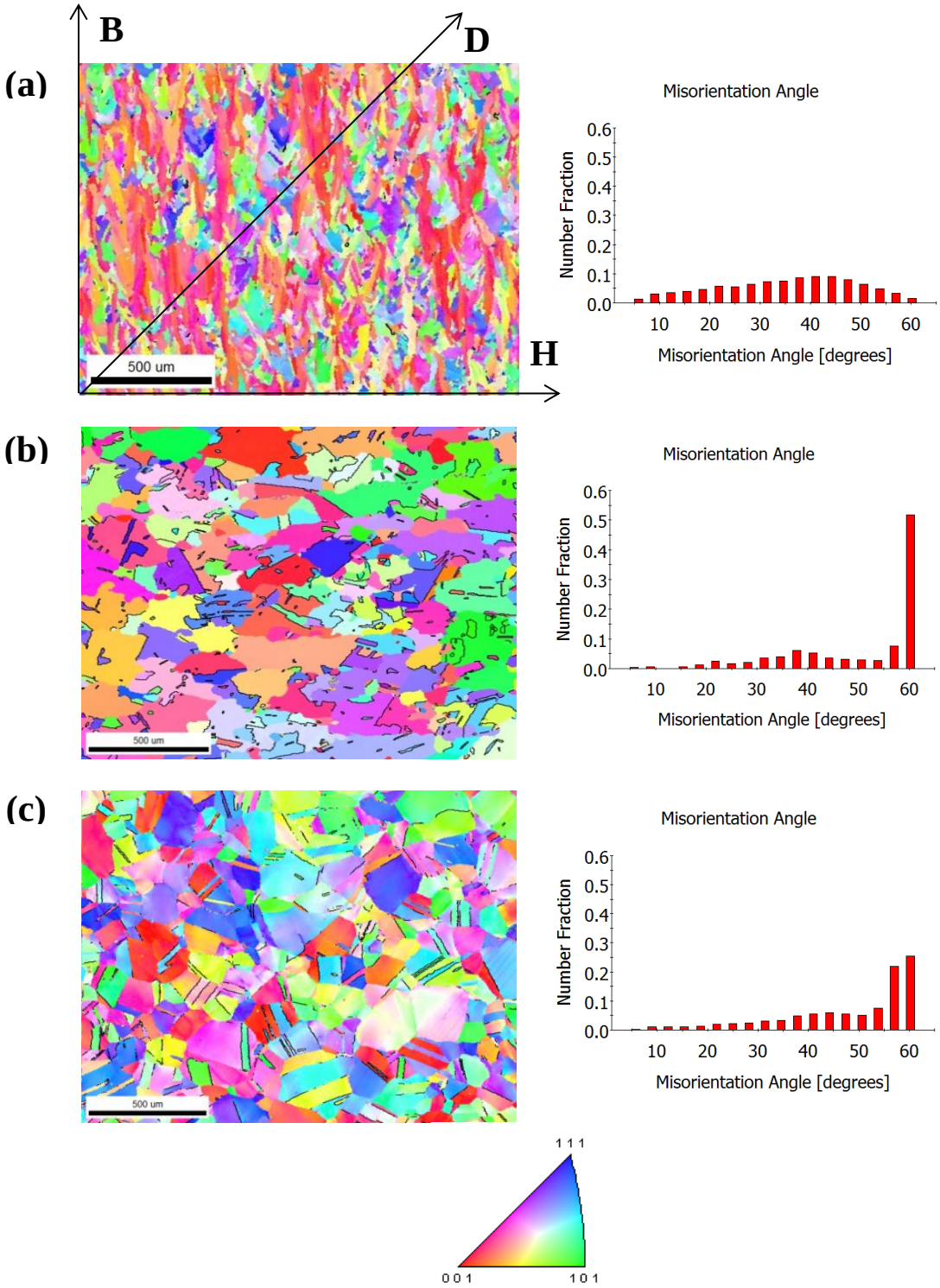

Figure II.1. Orientation maps showing the microstructure in the samples of Inconel 718 in different condition: (a) DMLS and double-aged, (b) DMLS, double aged and HIPed, and (c) wrought and double-aged. The colors in the maps indicate the orientation of the vertical axis with respect to the crystal reference frame according to the inverse pole figure (IPF) triangle. The scale bar of 500 μm is the same for all the maps. Comparison of grain boundary types in the samples is also shown. Twin boundaries for the annealing twin in the maps are highlighted within the maps in black.

The DMLS followed by double-aging processed samples show elongated grain structure in the build direction with an approximate aspect ratio of four. As a result, the samples machined in the H direction have a different initial microstructure from the samples machined in the D direction. Crystallographic texture is a <100> fiber of a moderate strength aligned with the build direction [19]. Content of annealing twins is very small as revealed by the misorientation plot. The microstructure in terms of the porosity content was characterized using micro X-ray computed tomography (μXCT) in the earlier work [19], and found to contain approximately 0.18% of porosity. The estimate was regarded as the lower bound.

The DMLS followed by double aging and HIPing processed samples show equiaxed grain structure and a high content of annealing twins. This finding is important as coherent twin boundaries (60^{o}) are known to be detrimental to fatigue performance of the material. A recent study on fatigue cracks in a Ni superalloy revealed that all the cracks were effectively coincident with coherent twin boundaries [37]. The HIPed material is not supposed to contain any porosity.

Wrought and double-aged samples show the typical equiaxed grain structure with some fraction of the twin boundaries, which is much less than in the HIPed material. The grain size is also smaller than in the HIPed material.

The above three categories of the Inconel 718 samples with their associate microstructures are tested in low cycle fatigue and high cycle fatigue.

III. LOW CYCLE FATIGUE OF INCONEL 718

In this chapter, the low cycle fatigue (LCF) performance of direct metal laser sintered (DMLS) Inconel 718 superalloy is presented. The material was deposited in two directions, horizontally and diagonally (45°) with respect to the loading direction, heat treated, and hot isostatically pressed (HIP). Strain-controlled LCF tests were conducted under a mean strain of 0.5% and several strain amplitudes ranging between 0.6%-1.4%. To have a reference for the LCF behavior, a set of wrought Inconel 718 samples in the same condition was also tested, and the results compared against the results for the DMLS materials. As reported in Chapter II, this work was published in December 2016 in *International Journal of Fatigue*.

III.1. Low cycle fatigue specimen design

LCF testing was performed on the *MTS Landmark 270* servohydraulic testing system with Flextest software and controller. The load was recorded using a *MTS 661.22H-01* 250kN load cell with a maximum error of 0.35%. Specimen elongation was measured using a *MTS 634.12E-24* extensometer. Forces and displacements were then converted into engineering stresses and strains according to the following formulae

$$\sigma_{eng} = \frac{F}{A_0} \tag{III.1}$$

where σ_{eng} is the engineering stress, F is the force measured from the force sensor, and A_0 is the initial cross sectional area of the specimen and

$$\varepsilon_{eng} = \frac{\Delta l}{l_0} \tag{III.2}$$

where ε_{eng} is the engineering strain, Δl is the displacement measured by the extensometer, and l_0 is the extensometer gage length.

True stresses and strains can be found by the formulae

$$\sigma_t = \sigma_{eng} \cdot (1 + \varepsilon_{eng}) \tag{III.3}$$

and

$$\varepsilon_t = \ln(1 + \varepsilon_{eng}) \tag{III.4}$$

The low cycle fatigue specimens were designed in accordance with ASTM E606 with a modification to the grip section to fit into the existing flat hydraulic grips, as shown in Figure III.1 [38]. The specimen gage section is 0.5 in. (12.7 mm) long and 0.25 in. (6.35 mm) in diameter.

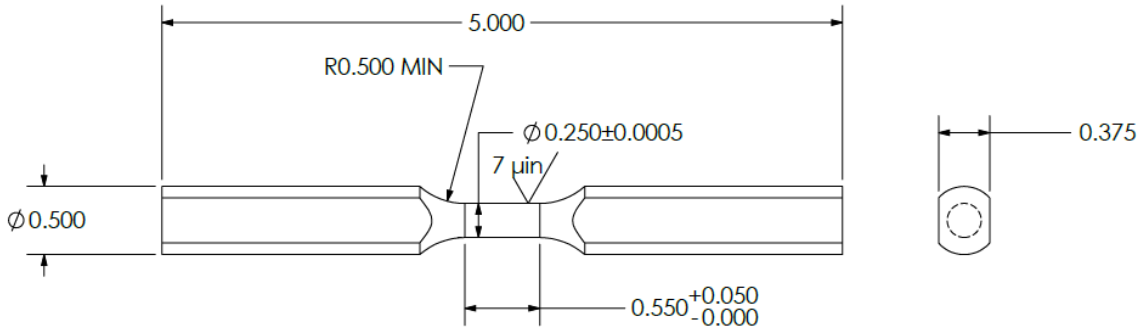

Figure III.1. Low cycle fatigue specimen geometry with dimensions in inches.

Material for the DMLS samples was printed at Turbocam International in two orientations with respect to build direction (BD): diagonal at 45° (D), and horizontal (H), as shown in Figure III.2.

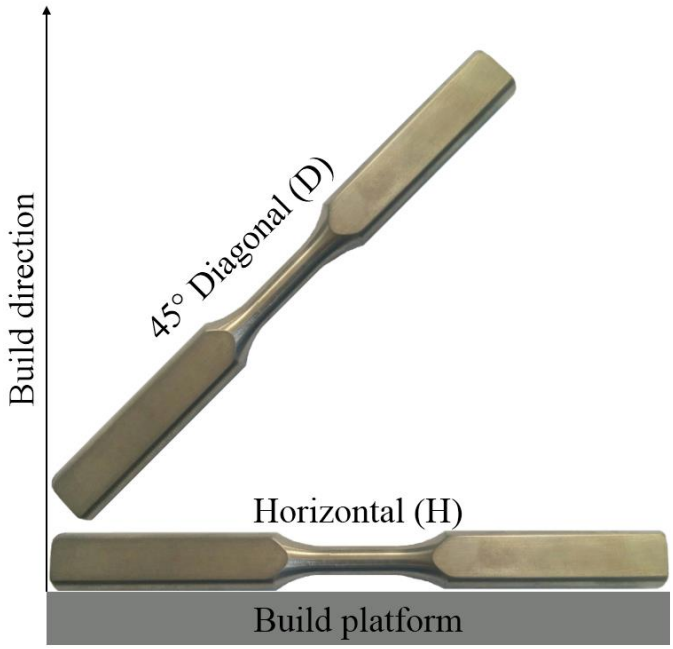

Figure III.2. Orientation of low cycle fatigue samples with respect to the build direction (BD).

Since the available extensometer had a nominal gage length of 1 in. (25.4 mm), as seen in Figure III.3a, gage-length "de-extenders" were manufactured and attached to shorten the gage length to 0.5 in. (12.7 mm). The final extensometer used in the tests is shown in Figure III.3b.

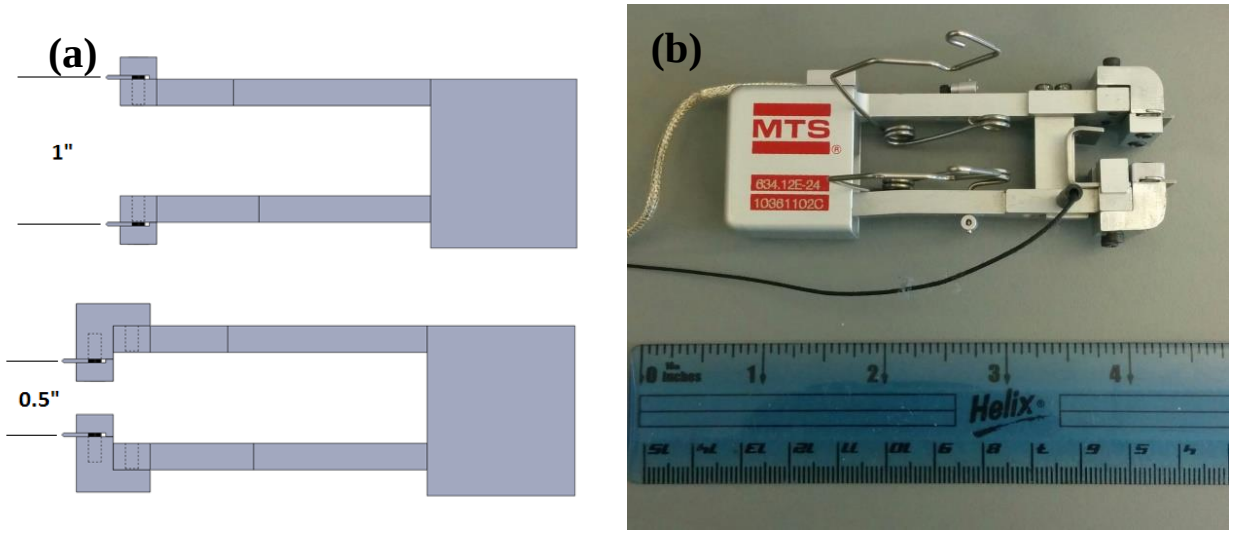

Figure III.3. (a) Schematic of the MTS 634.12E-24 extensometer modified to fit the 0.5 in. (12.7 mm) gage length. (b) Modified 0.5 in. (12.7 mm) gage length extensometer.

III.2. Preliminary studies on steel specimens

DMLS specimens are expensive to manufacture and only a limited number of specimens were available for the studies. Thus, steel tension and LCF specimens were manufactured to perform preliminary cyclic tests and investigate different methods of checking for specimen buckling. The steel *tension specimen* gage section was 1in. (25.4 mm) long and 0.35 in. (8.9 mm) in diameter. The steel *LCF specimen* had the same dimensions as the specimen shown in Figure III.1.

Figure III.4. Steel tension and LCF specimens for preliminary testing.

Figure III.5 shows the stress-strain response for the steel specimen in *tension* tested under displacement control with a strain rate of about $4.5 \times 10^{-4}\, s^{-1}$. Based on the test data, the Young's modulus was calculated as 211 GPa. The 0.2% offset yield strength and ultimate tensile strength (UTS) were found to be 683 MPa and 744 MPa, respectively.

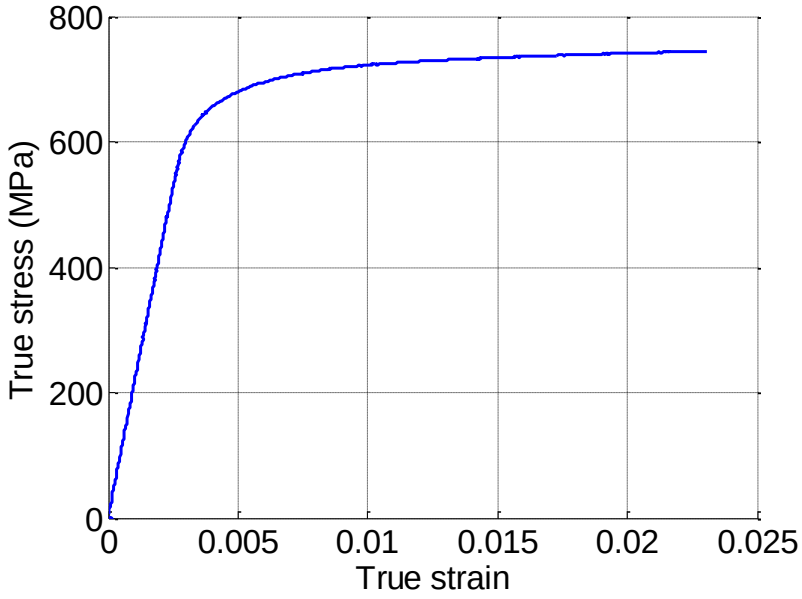

Figure III.5. Stress-strain curve for the steel specimen in tension.

In order to investigate methods of detecting buckling in the specimen, a cyclic incremental strain test was performed on a steel *LCF specimen*. The specimen was cycled to increasing amounts of strain up to 8% and unloaded to zero strain as shown in Figure III.6. The test was run at a displacement rate of 0.0127 mm/s corresponding to a strain rate of about $5 \times 10^{-4}\ s^{-1}$.

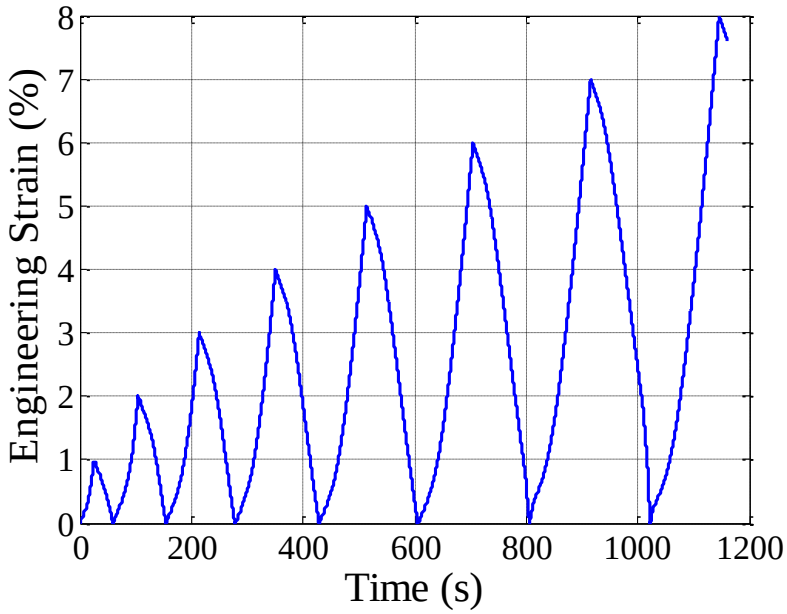

Figure III.6. Incremental strain test procedure performed on a steel specimen.

The stress-strain response is shown in Figure III.7. The steel underwent cyclic softening throughout the test. Figure III.8 shows the last two cycles of the incremental strain test. One can observe a sudden change in slope during the reloading of the specimen from zero strain, highlighted by the red circle. It is assumed that the specimen buckled and the first portion of reloading was the specimen straightening. Once the specimen straightens, the apparent stiffness increased, causing the change in elastic slope as seen in the figure.

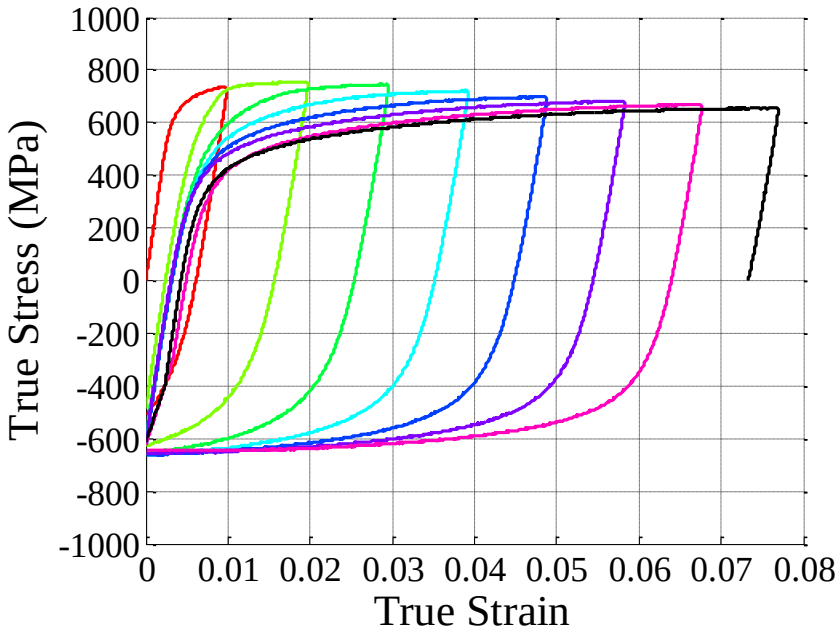

Figure III.7. Stress-strain response for the incremental strain test up to the 8% strain cycle.

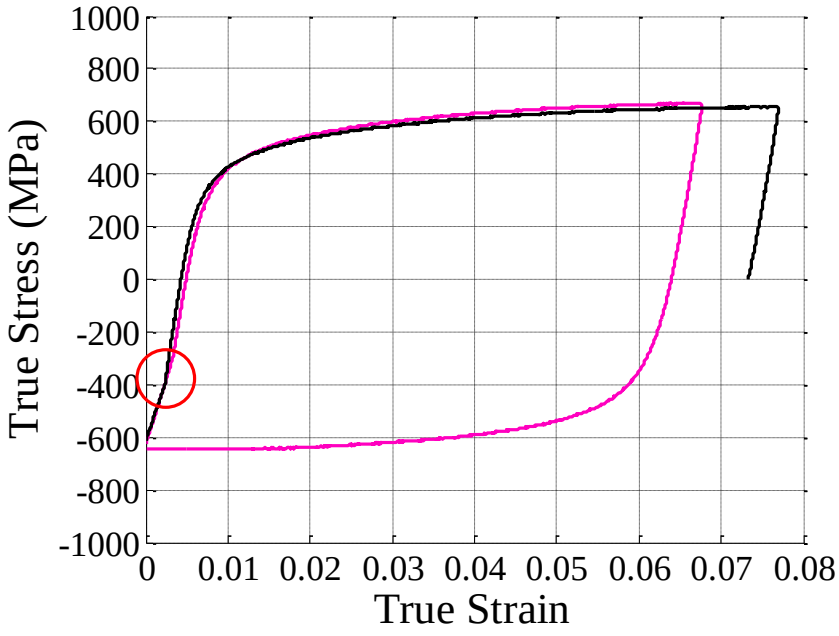

Figure III.8. The last two cycles of the incremental strain test.

It is important to reduce the amount of bending in the specimen as much as possible for axial LCF tests. One method of detecting specimen alignment or buckling, outlined in ASTM E1012, is to measure the bending strain in the specimen during loading. This is achieved by mounting 4 strain gages at 90° increments around the circumference of the cylindrical gage section of the specimen as shown in Figure III.9.

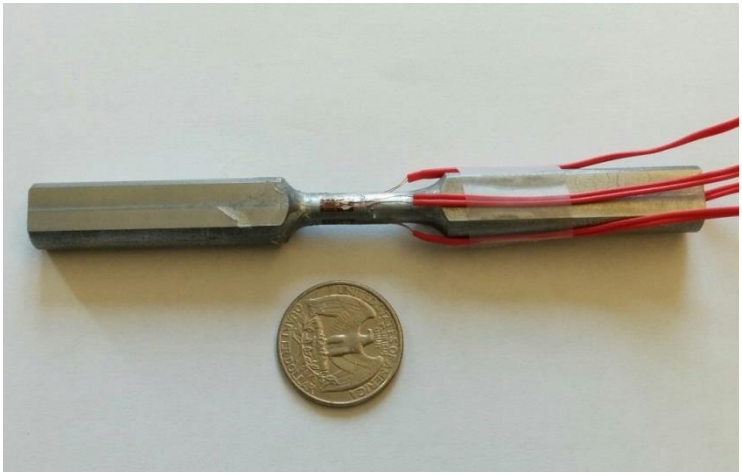

Figure III.9. Strain gages mounted to a steel LCF specimen at 90° increments to measure specimen bending.

By comparing the strains measured at each strain gage to the nominal strain of the gage section, the bending strain of the specimen can be calculated. Figure III.10 shows the strains recorded from the strain gages and their average compared to the data from the extensometer. The strain gages debonded after 3% strain and data collection was stopped.

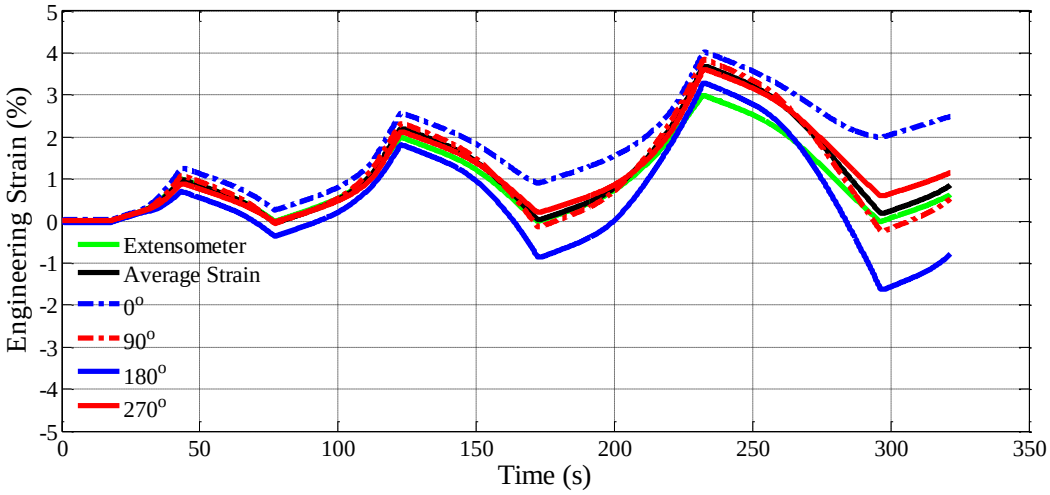

Figure III.10. Strain measurements recorded from the strain gages compared to the strain measured from the extensometer.

It can be seen that from the start of the test, the strains measured by the strain gage deviate from each other. This indicates that there is a possibility of some bending in the specimen as it is loaded. The average of the strain gage measurement, which is the nominal strain of the gage section, doesn't match the strain measured using the extensometer. The most probable cause for this is misalignment in the strain gages with respect to the loading direction of the specimen, although it is unclear which of the 4 gages were not aligned properly.

In order to quantify the amount of bending in the specimen, the average strain is subtracted from the strains for each of the 4 strain gages. These bending strains are plotted in Figure III.11. It can be seen that there is fully reversed bending in the 90° and 270° strain gages as the signs of the bending strains reverse, while there is no tension-compression reversal exhibited by the 0° and 180° strain gages. Overall, the data doesn't provide any consistent indication of the presence or absence of bending.

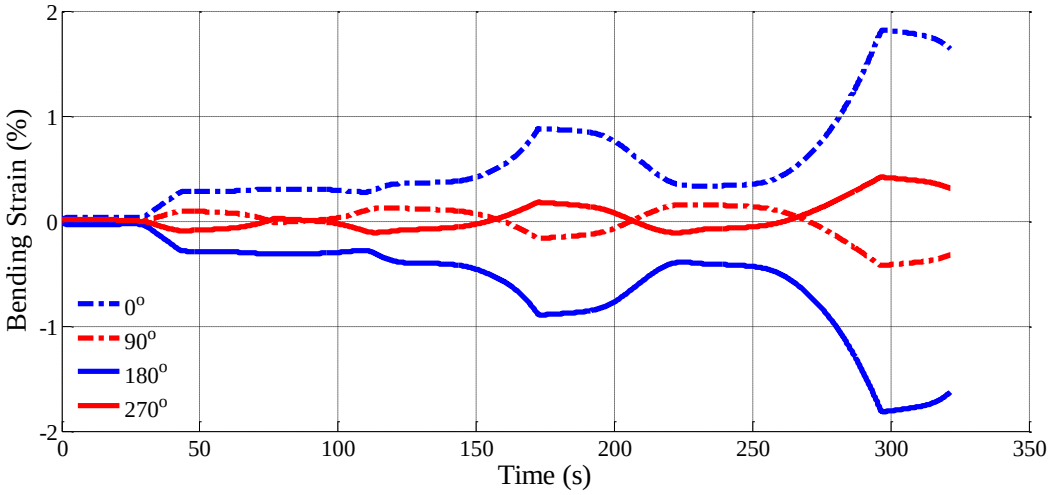

Figure III.11. The bending strains captured by the strain gages for the incremental strain test.

Based on these results, the use of strain gages to check for specimen misalignment for low cycle fatigue tests was deemed unreliable, as they present too many sources of error to be trusted. Thus, evidence of buckling must be observed though analysis of the stress-strain response of the material. Any deviation from the expected response is assumed to be the effect of specimen misalignment or buckling.

III.3. Monotonic tests on low cycle fatigue Inconel 718 specimens

To quantify the limits of the low cycle fatigue testing procedure, preliminary tension and compression tests were performed on the LCF specimens. Figure III.12 shows the results of tension tests performed on the LCF specimens for the HIPed DMLS and wrought materials compared to tension tests performed on Diagonal and Horizontal DMLS materials by Smith et al. [19]. As seen, the samples made by DMLS and double aged (HT) exhibit the highest strength. However wrought and HIPed samples exhibit more elongation before failure.

In Smith et al. [19], it was observed that the DMLS Inconel 718 shows tension-compression asymmetry. To test the alignment of the specimen and investigate whether buckling could be observed using the stress-strain response, a group of LCF specimens were compressed and their stress-strain responses compared. Figure III.13 shows the test results for the HIPed and wrought specimens.

As seen, the stress-strain response in compression drops below the curve in tension, which is evidence that the specimen has buckled. In Figure III.13b, it can be seen that the material preserves the integrity without buckling up to at least 1.5% strain in compression. Even though a positive mean strain of 0.5% was chosen to ensure no sample buckling during low cycle fatigue experiments with the considered strain amplitude range.

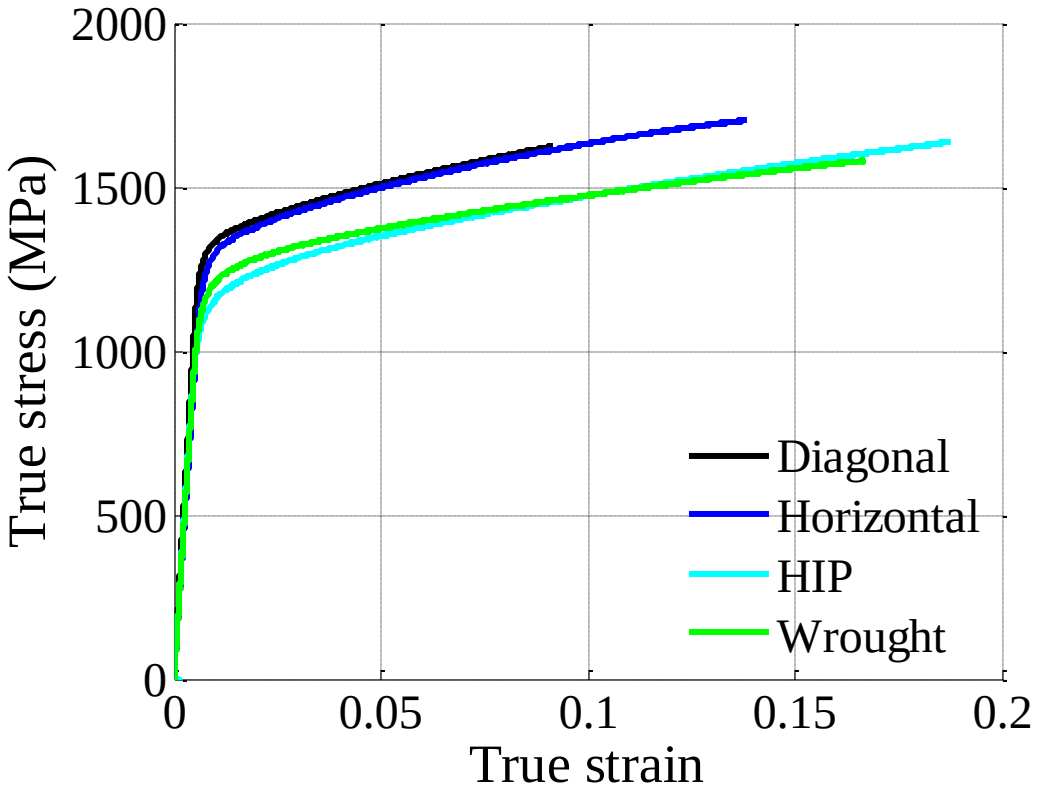

Figure III.12. True stress- true strain response in tension measured using the LCF specimens for the studied materials.

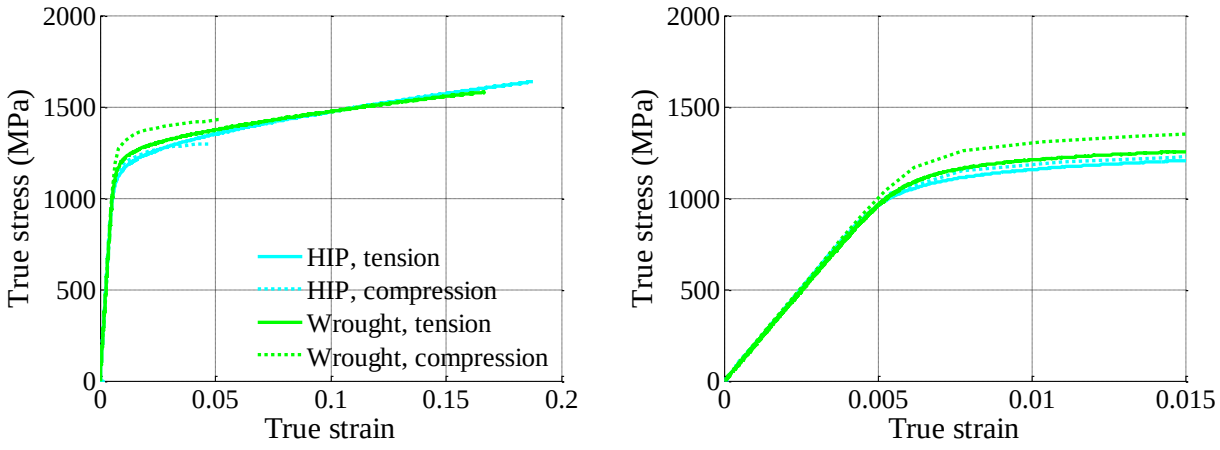

Figure III.13. (a) Tension-compression asymmetry for the HIPed and wrought specimens. (b) Zoom in into the response up to about 1.5% strain.

III.4. Inconel 718 low cycle fatigue testing procedure

To investigate the fatigue properties of Inconel 718, strain controlled low cycle fatigue experiments were conducted. Specimens were subjected to tension – compression cyclic loading at constant strain amplitudes, ε_a, of either 0.6%, or 0.8%, or 1.0%, or 1.2%, or 1.4% as shown in Figure III.14. The number of cycles to failure, N_f, was recorded. A positive mean strain was used in the experiments to help prevent buckling during the compressive stage of cyclic loading as routinely used in low cycle fatigue experiments [39–41]. The value of 0.5% was selected for the reported tests based on preliminary monotonic studies described in section 0. Experiments were performed on differently manufactured and treated Inconel specimens as shown in Table III.1.

Table III.1. Strain amplitudes of the low cycle fatigue experiments.

DMLS (D, HT)	DMLS (H, HT)	Wrought (HT)	DMLS (H, HT, HIP)
Strain Amplitude	Strain Amplitude	Strain Amplitude	Strain Amplitude
0.60%	0.60%	0.60%	--
0.80%	0.80%	0.80%	--
1.00%	1.00%	1.00%	1.00%
1.20%	1.20%	1.20%	1.20%
1.40%	1.40%	1.40%	--

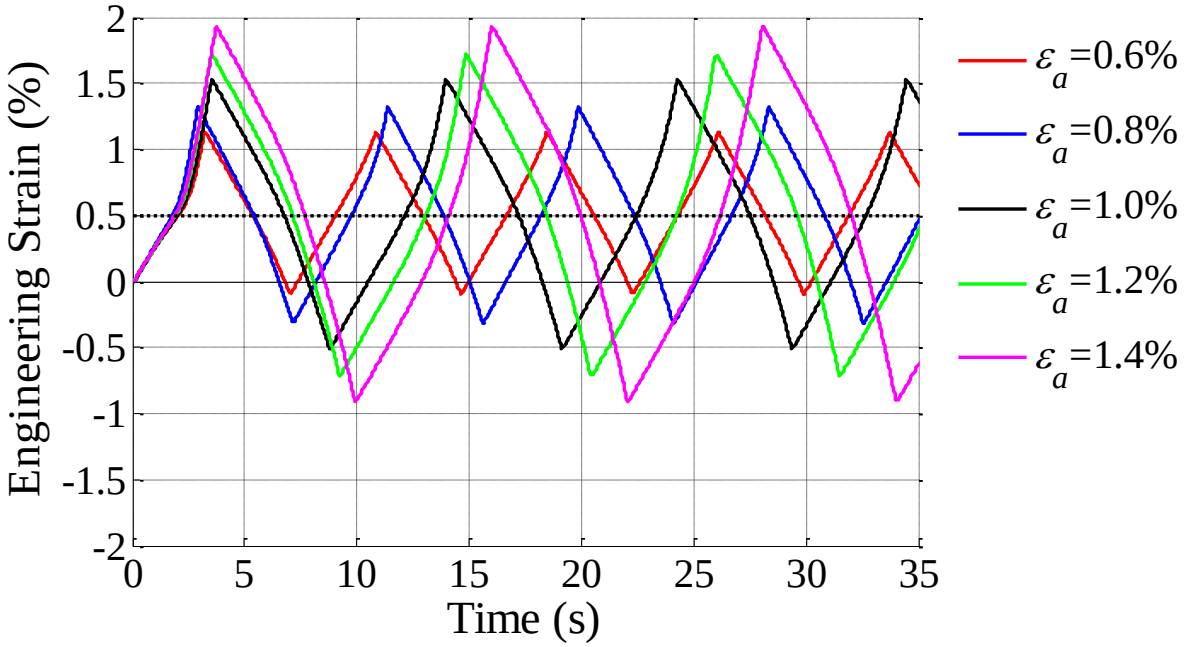

Figure III.14. Low-cycle fatigue push-pull waveforms used in testing. The applied mean strain is ε_m = 0.5% for all and the amplitude strains are indicated in the legend.

LCF tests were performed using displacement control with strain limits controlled using the extensometer. Strain rates were approximately $4 \times 10^{-3}\ s^{-1}$ and frequency approximately 0.15 Hz.

III.5. Results of low cycle fatigue of Inconel 718

The number of cycles to failure for strain amplitudes ranging from 0.6% to 1.4% is shown in Figure III.15. As expected, N_f decreases with increase of the strain amplitude for each material category.

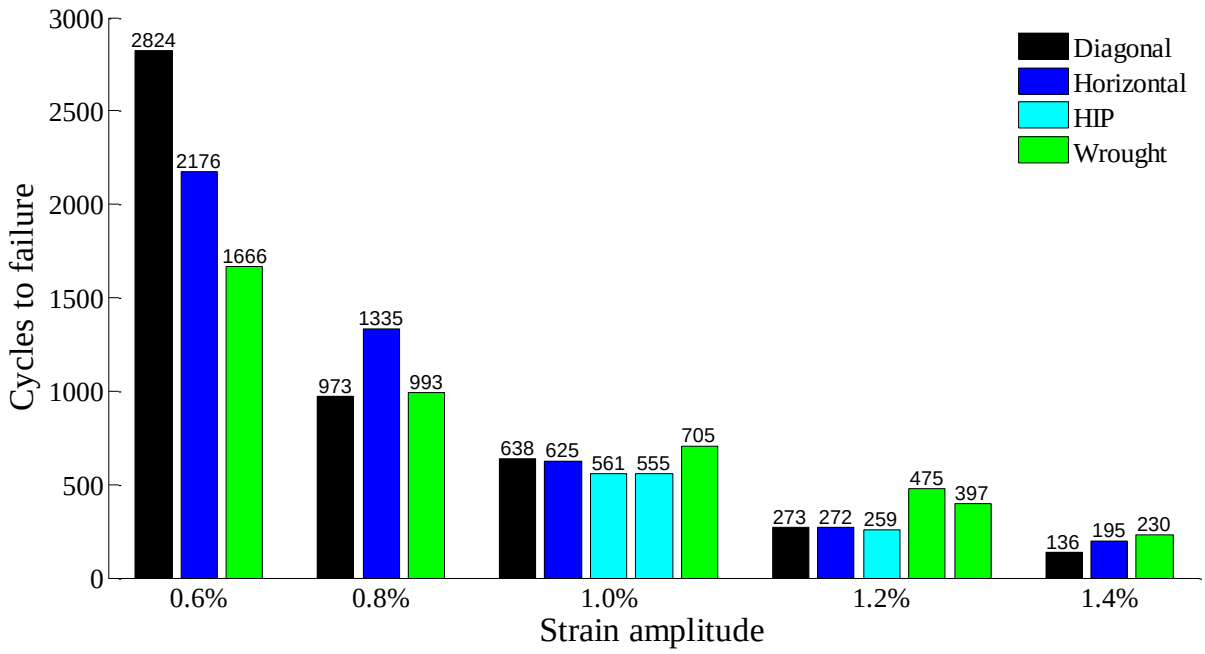

Figure III.15. Number of cycles to failure for the samples of Inconel 718 manufactured and treated as indicated in the legend.

The stress-strain responses for selected cycles over the life of the specimens are shown in Figure III.16 for the 1.2% strain amplitude. As can be seen, for each of these materials, there is initial cyclic hardening of the material in the first several cycles followed by a regime of softening until the fracture. The dislocation structure formation processes underlining this behavior have been reviewed in [42, 43]. The failure of the DMLS samples was always abrupt, while the wrought material exhibited a gradual failure.

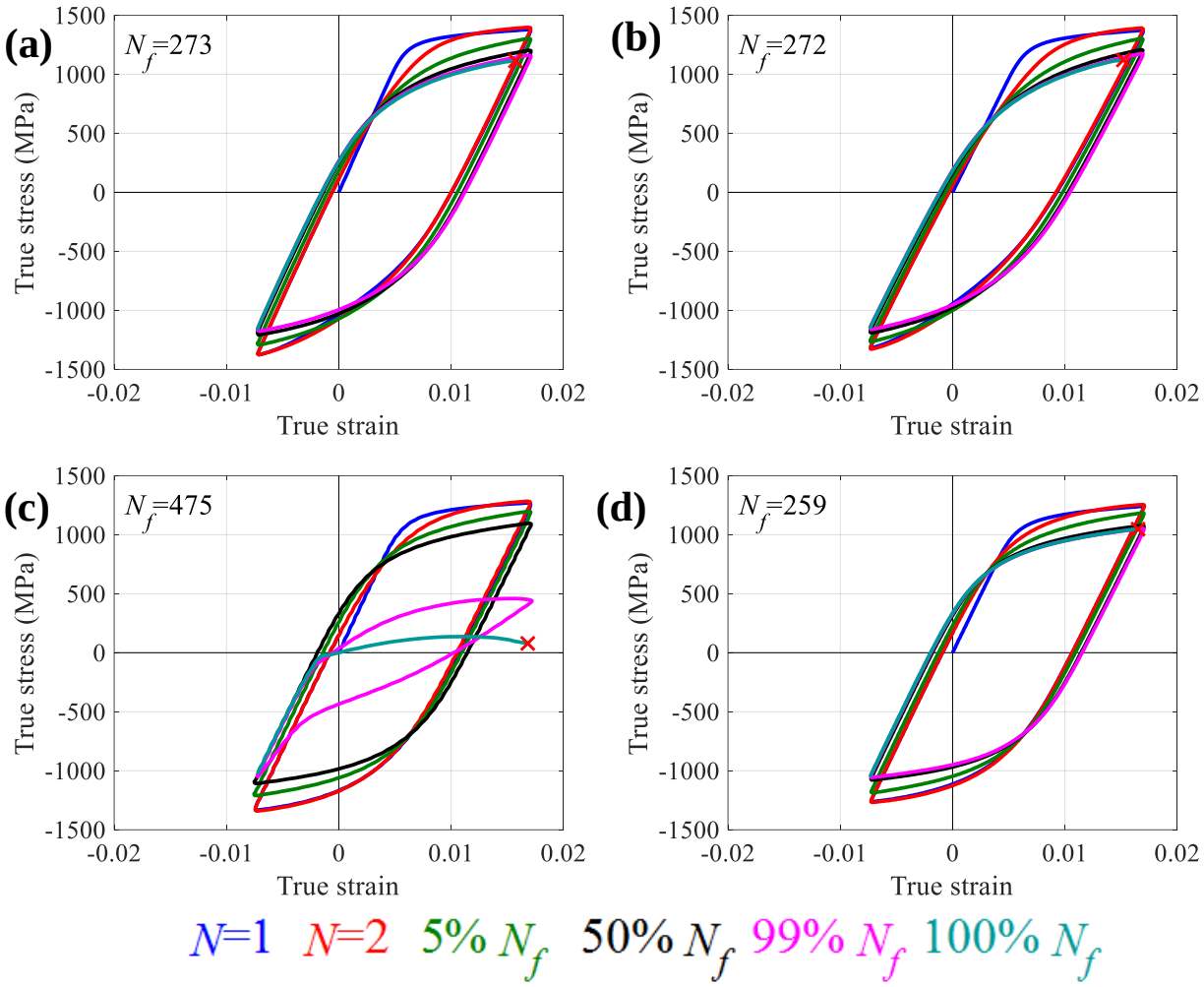

Figure III.16. 1.2% strain amplitude stress-strain hysteresis loops for (a) DMLS double aged diagonal (b) DMLS double aged horizontal (c) wrought double aged and (d) HIPed samples.

Figure III.17 shows the stress-amplitudes for each strain-amplitude tested. Here it can be seen that the DMLS diagonal sample exhibits the highest amplitude stress over all the other tested samples during the life of the specimens. None of the curves shows stable cyclic stress amplitude. The cyclic softening is increasing with the strain amplitude. For most of the samples tested, the specimen underwent a sudden "brittle" failure with rapid crack propagation. Interestingly, failure of the wrought specimens was not so abrupt.

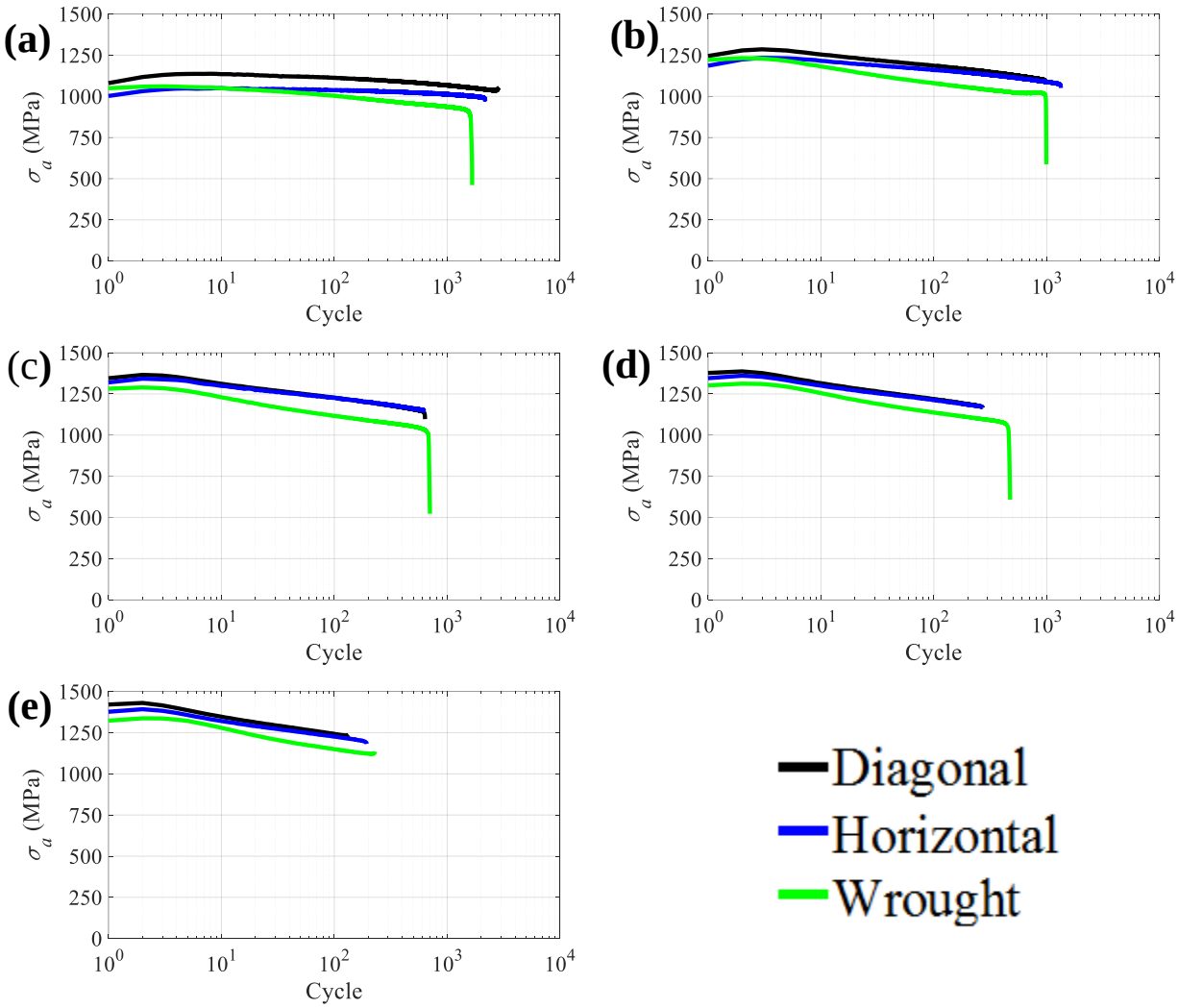

Figure III.17. Stress-amplitudes for DMLS diagonal, DMLS horizontal, and wrought materials for strain amplitudes of (a) 0.6% (b) 0.8% (c) 1.0% (d) 1.2% and (e) 1.4%.

Figure III.18 shows the mean stress, σ_m, for each strain-amplitude tested. It can be seen that for the larger strain amplitudes, the mean stress is almost immediately accommodated by plastic deformation and approaches zero with continuation of the test. Moreover, it becomes compressive for the wrought material. This is a direct consequence of the tension-compression asymmetry exhibited by the material with the compressive strength being higher than the tensile strength

(Figure III.13). Compressive σ_m is highly desirable for extending the fatigue life. For lower strain-amplitude tests the mean stress is present and is decreasing throughout the duration of the test.

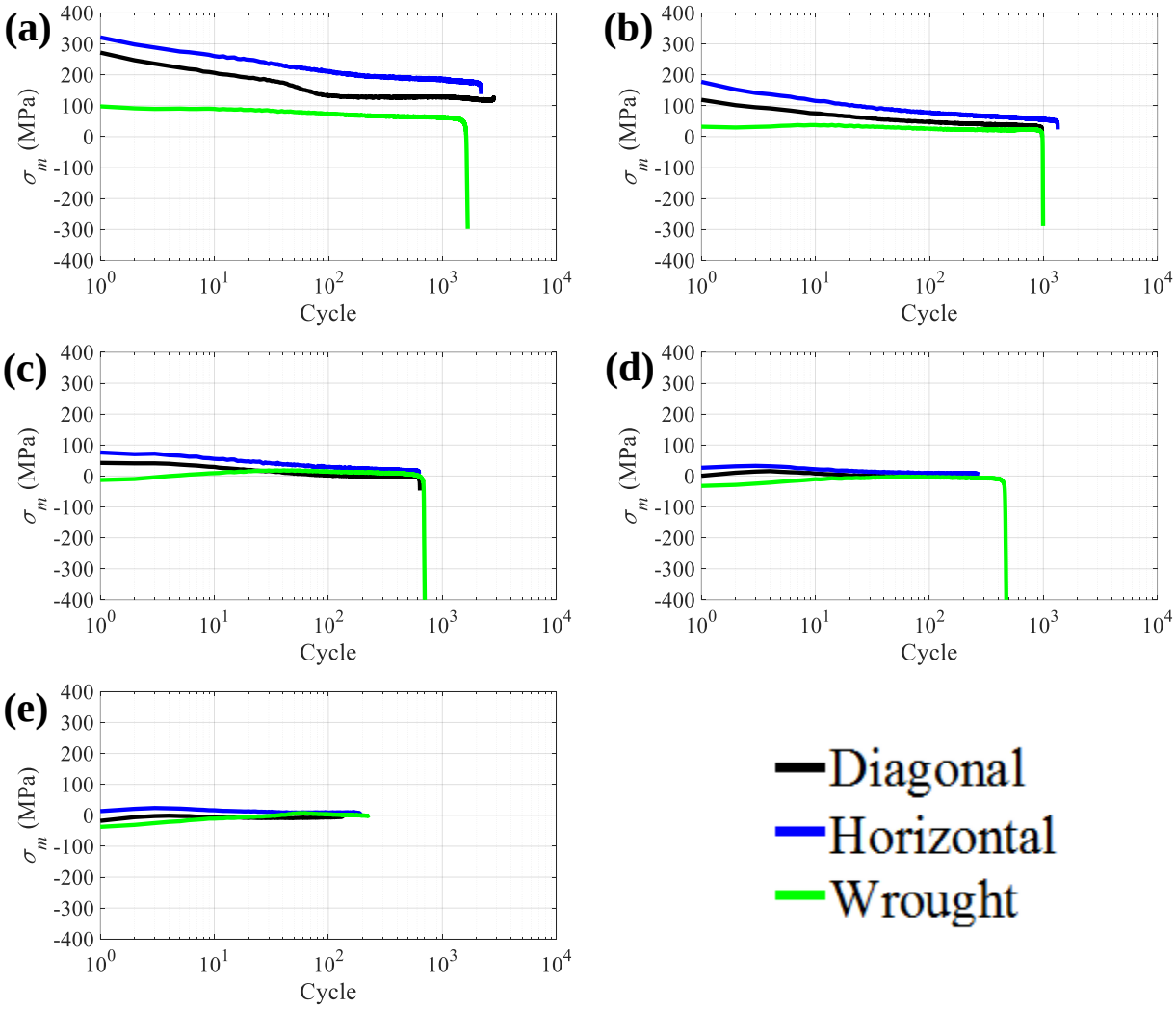

Figure III.18. Evolution of mean stress during the tests for the materials indicated in the legend under strain amplitudes of: (a) 0.6% (b) 0.8% (c) 1.0% (d) 1.2% and (e) 1.4%.

Figure III.19 shows the reduction in elastic modulus from the first cycle to the half-life of the specimen. Generally, as the strain amplitude is increased, the more reduction there is in elastic properties. It is assumed that the accumulation of residual stresses in the material accounts for this reduction in elastic modulus.

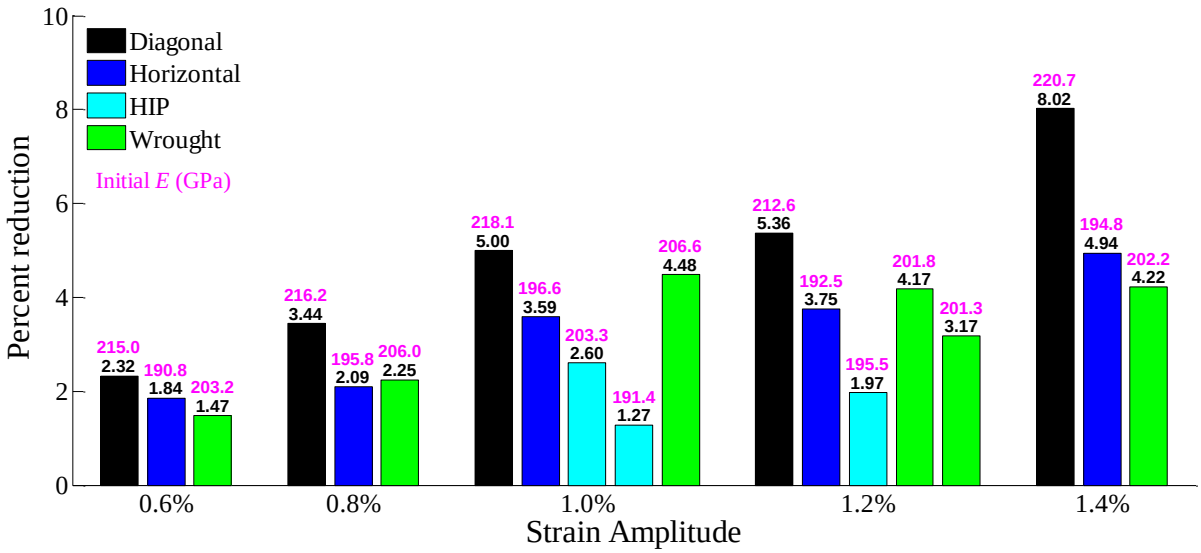

Figure III.19. Reduction in elastic modulus to the half-life of the LCF specimens.

The DMLS HT material is stronger in simple tension than the wrought HT material, which is likely due to a finer grain structure. However, the DMLS HT material is not as ductile as the wrought HT material. The limited ductility exhibited by the DMLS HT samples is due to the presence of porosity, which is absent in the wrought HT material. The diagonal DMLS HT samples exhibit a slightly higher strength than the horizontal DMLS HT material. This is due to the grain shape effects relative to the loading direction. The mean free path of dislocations moving along the loading direction is longer in the diagonal than in the horizontal sample grain structure. The longer the mean free path of dislocations, the less hardening is accumulated in the material [44–47]. Finally, the curve of the HIPed DMLS material is below the DMLS HT material curves likely due to coarser grain structure, but ductility of the HIPed material has substantially increased. The loss of ductility in the DMLS HT samples is due to the presence of porosity, which is supposed to be eliminated in the HIPed material. After HIP, the microstructure transforms from being elongated to be equiaxed, and the grain size is much coarser as compared to the grain size of DMLS

HT material (Figure II.1). Additionally, the fraction of grain boundaries associated with annealing twin substantially increases after HIP.

Consistently with the behavior of the wrought HT material, the number of cycles to failure for the DMLS HT material decreases with the increase of strain amplitude. However, the rate of this decrease for the DMLS HT material is higher than for the wrought HT material. Such behavior is likely due to the presence of porosity, which is absent in the wrought material [21]. For lower strain amplitudes, the porosity in the DMLS HT material does not play as much of a role in the degradation of the material as it does for higher strain amplitudes. Therefore, the deformation of the material at small strains, which is just above the initial yield stress, is not as much influenced by the porosity as it is later in the plastic region, where strain hardening is playing a significant role. As a result, the DMLS HT material, which has a higher strength, also has a longer LCF life than the wrought HT material for low strain amplitudes. The diagonal DMLS HT material has a longer life than the horizontal DMLS HT material since it has a slightly higher strength due to grain structure. As the strain amplitudes increase, the plastic deformation mechanisms and the underlying ductility becomes more important. Therefore, the more ductile wrought material exhibits better fatigue performances.

Although the HIPed material appears to be as ductile as the wrought material, its LCF behavior is not as good. The shorter life of the HIPed material for the same strain amplitude can be explained by large content of annealing twins in its microstructure. The coherent twin boundaries shorten fatigue life of the material because fatigue cracks in a nickel-based superalloy are known to nucleate and propagate along the coherent annealing twin boundaries [26].

III.6. Coffin-Manson strain-life prediction

The strain-life data for LCF can be approximated by the Coffin-Manson relation [20, 48]. Here, the strain amplitude ε_a is broken up into elastic and plastic components

$$\varepsilon_e = \left(\frac{\sigma_a}{E}\right)_{50\%}, \tag{III.5}$$

$$\varepsilon_p = \varepsilon_a - \varepsilon_e, \tag{III.6}$$

where ε_e is the elastic strain amplitude, σ_a and E are the stress amplitude and elastic modulus at 50% of the specimen's life, and ε_p is the plastic strain amplitude.

The elastic and plastic components of strain amplitude are plotted against N_f in a log-log scale. These data points are then fitted with the Coffin-Manson relations [49–51]

$$\varepsilon_e = \frac{\sigma_f'}{E}\left(2 \cdot N_f\right)^b, \tag{III.7}$$

$$\varepsilon_p = \varepsilon_f'\left(2 \cdot N_f\right)^c, \tag{III.8}$$

where σ_f' is the fatigue strength coefficient, E is the elastic modulus during the initial loading per specimens category, b is the fatigue strength exponent, ε_f' is the fatigue ductility coefficient, and c is the fatigue ductility exponent. Since the data is plotted in a log-log scale, the Coffin-Manson model becomes linear, with b and c as the slopes and $\frac{\sigma_f'}{E}$ and ε_f' as the intercepts for the elastic and plastic curves, respectively. Here, the value of E at 50% life cannot be used since E changes depending on the strain amplitude (see Figure III.19). Note that (3) and (4) are used to describe strain life behavior based on a set of experiments conducted at different strain amplitudes.

The measured data for the DMLS HT material is plotted in Figure 8 along with available literature data for Inconel 718 in the same condition [20] and the strain-life Coffin Manson curves for generic Inconel from Dowling [48]. Note that the literature data was provided for the fully reversed strain cycles.

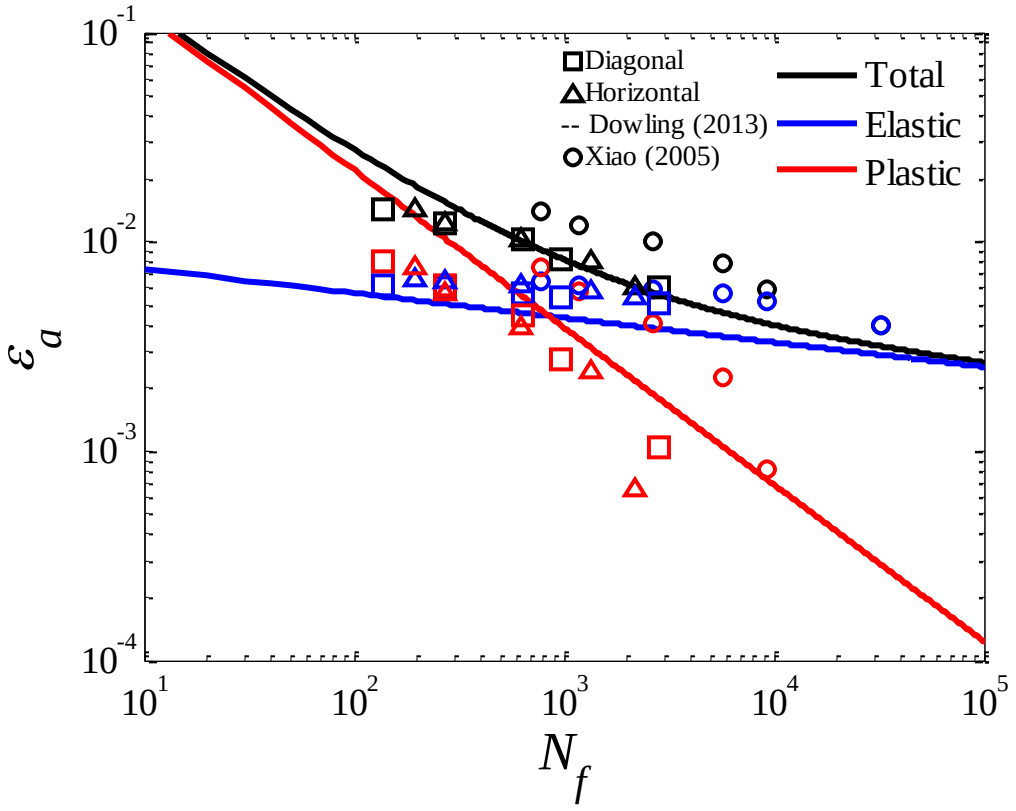

Figure III.20. Total, elastic, and plastic strains for horizontal and diagonal DMLS double-aged specimens tested here compared to the literature data in Dowling [48] and Xiao et al. [20].

It can be seen that the Coffin-Manson parameters from Dowling [48] do not accurately describe all the tested material conditions. As shown earlier, elastic and plastic properties vary with the difference in initial microstructure between the H-built and D-built DMLS as well as the wrought material conditions. Therefore, in this work we establish the Coffin-Manson coefficients separately

for each condition of the material. The individual strain-life curves are plotted in Figures III.21-III.23.

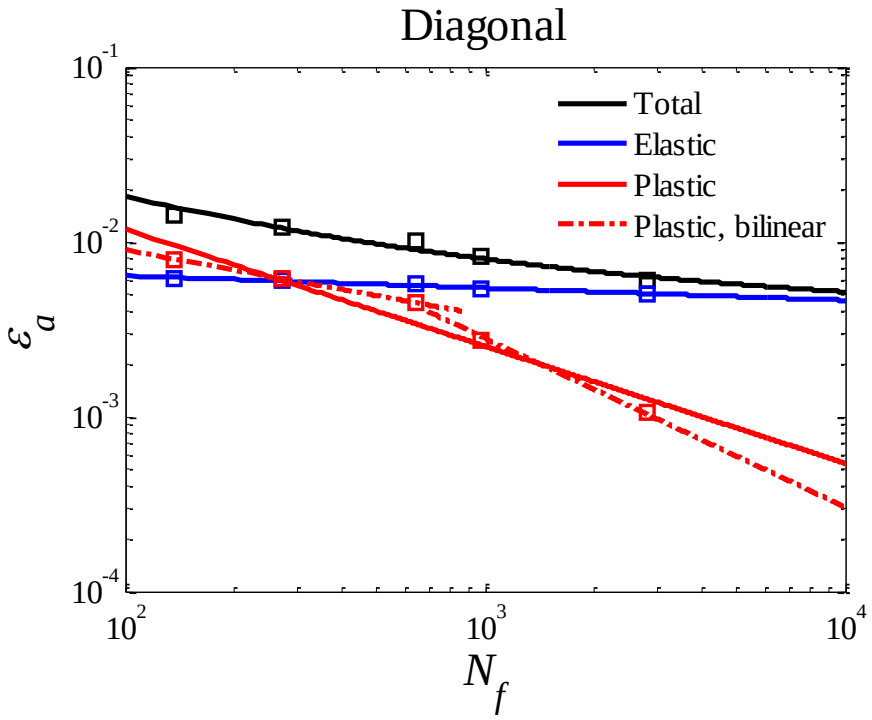

Figure III.21. The Coffin-Manson model fit of the measured data for the D-built DMLS Inconel 718 in the double-aged condition.

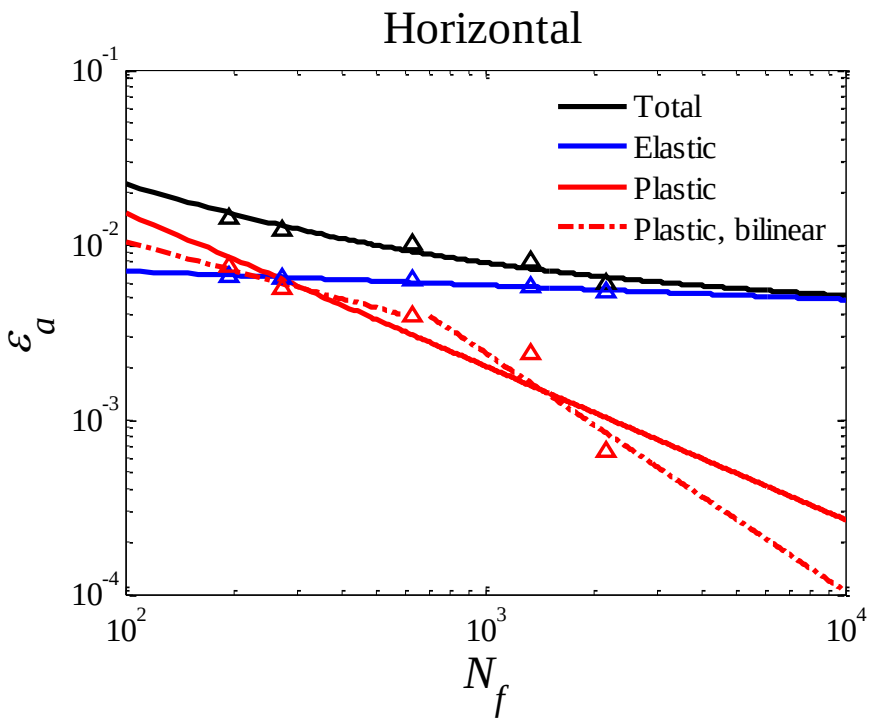

Figure III.22. The Coffin-Manson model fit of the measured data for the H-built DMLS Inconel 718 in the double-aged condition.

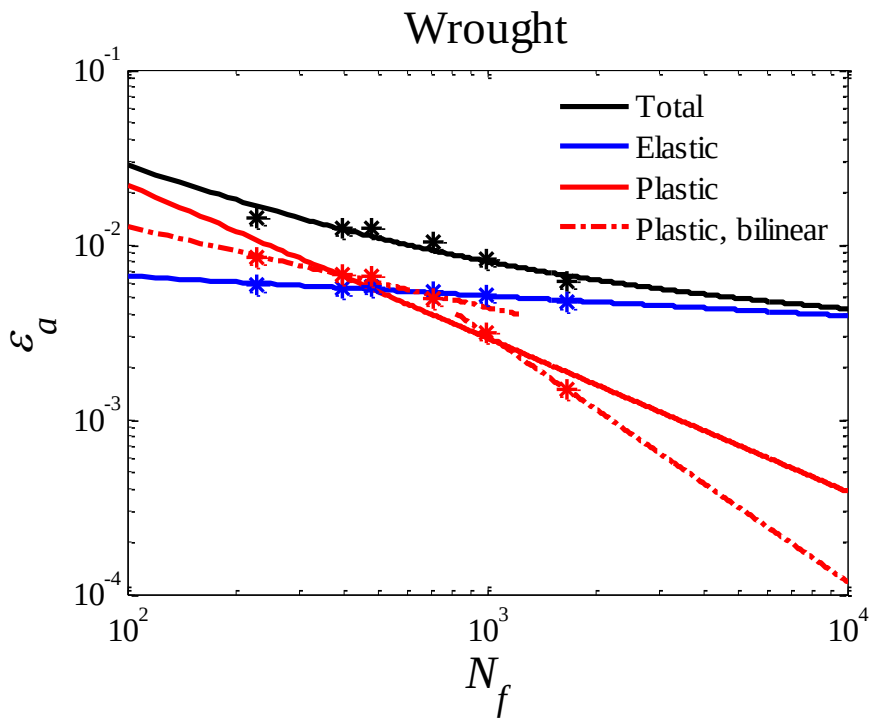

Figure III.23. The Coffin-Manson model fit of the measured data for the wrought Inconel 718 in the double-aged condition.

Figures III.21-III.23 present two choices for the $\varepsilon_p - N_f$ curve fit. The first choice, shown as a solid line, corresponds to the traditional formulation of the Coffin-Manson model when results are fitted over the entire range of plastic strain amplitudes. However, as was observed in Xiao at al. [20], there is an inflection point in the $\varepsilon_p - N_f$ relation for plastic strain amplitudes below 0.4%. For this reason, Xiao at al. [20] proposed an extended Coffin-Manson relation for the $\varepsilon_p - N_f$ curve, which is a bilinear fit in the log-log scale. The same inflection point was observed for all the tested materials in this work, and thus the bilinear fit better describes the data. These bilinear fit curves are plotted as dashed lines in Figures III.21-III.23.

The parameters used to create the Coffin-Manson curves are presented in Table III.2.for the full range and Table III.3 for the extended bilinear fits. The correction coefficients demonstrate that the data is well represented by the fits.

Table III.2. Parameters of the Coffin-Manson model for the DMLS and wrought Inconel 718.

	E (GPa)	σ_f' (MPa)	b	ε_f'	c
Dowling (2013)	214	2255	-0.117	1.16	-0.749
Diagonal	216.51	2011.2	-0.0704	0.4014	-0.6670
Horizontal	193.94	2115.7	-0.0819	1.5919	-0.8773
Wrought	203.51	2463.4	-0.1141	2.2793	-0.8763

Table III.3. Parameters of the bilinear Coffin-Manson model for the DMLS and wrought Inconel 718.

	$\varepsilon_p \geq 0.40\%$			$\varepsilon_p \leq 0.40\%$		
	ε_f'	c	Correlation Coefficient	ε_f'	c	Correlation Coefficient
Diagonal	0.0652	-0.3745	0.9999	4.2027	-0.9622	0.9965
Horizontal	0.1821	-0.5410	0.9708	74.454	-1.3606	0.8660
Wrought	0.1458	-0.4614	0.9450	134.879	-1.4076	0.9986

DMLS can potentially reduce the cost of manufacturing complex geometry parts. This work showed that Inconel 718 manufactured by DMLS exhibits strength and LCF properties comparable to those of Inconel 718 traditionally manufactured by forging. Specifically, DMLS material lasts longer in LCF than the wrought material in the same condition at low but not at high strain amplitudes. The behavior is rationalized in terms of the DMLS induced porosity present in the microstructure because its influence is not as significant at low strain amplitudes as it is at high strain amplitudes. We find that the HIP treatment deteriorates the LCF performance of the material due to a high content of annealing twins in the microstructure created during the HIP treatment. The presence of annealing twins in the microstructure has larger effect on shortening the life of the material than porosity at moderate to large strain amplitudes. The Coffin-Manson model was fit to delineate the strain-life curves for the studied materials. It was observed that at lower strain

amplitudes, where plastic strain is small, the standard Coffin-Manson model deviated from the data. An extended, bilinear, Coffin-Manson model for LCF was found to better represent the measured data for the considered range of plastic strain amplitudes. In summary, the work showed that porosity and inhomogeneities within grain structure such as non-uniform grain shape and annealing twins are yet to be reduced in the microstructure before DMLS becomes a comprehensively superior manufacturing method for components operating under complex loading.

IV. HIGH CYCLE FATIGUE OF INCONEL 718

In this chapter, the high cycle fatigue (HCF) performance of direct metal laser sintered (DMLS) Inconel 718 superalloy is presented. The material was deposited in two directions, horizontally and diagonally (45°) with respect to the loading direction, heat treated, and hot isostatically pressed (HIP). Stress-controlled rotary bending fatigue (RBF) tests were conducted under fully reversed loading with stress amplitudes ranging from 200 MPa to 1200 MPa. The results are compared with the data collected from a set of wrought Inconel 718 samples with the same heat treatment and available data on wrought Inconel 718 from literature.

IV.1. Rotating beam fatigue tester and high cycle fatigue specimen design

The machine used in this study is the rotating beam fatigue tester manufactured by Fatigue Dynamics, Inc. shown in Figure IV.1. The motor is controlled by a dial **(A)** which can vary the motor speed from 500 to 10,000 RPM (8.3 Hz to 166.7 Hz). The machine is capable of producing bending moments up to 200 in·lb by moving the poise weight **(C)** along a calibrated beam underneath the test platform. The machine also has a 2100 °F furnace **(E)** controlled by an *Omega CN3251* controller **(H)** which takes input from a Type K thermocouple mounted inside the furnace. A reservoir **(G)** pumps *Mobil Oil Co. Velocite 10* through the motor spindle to provide cooling throughout the test.

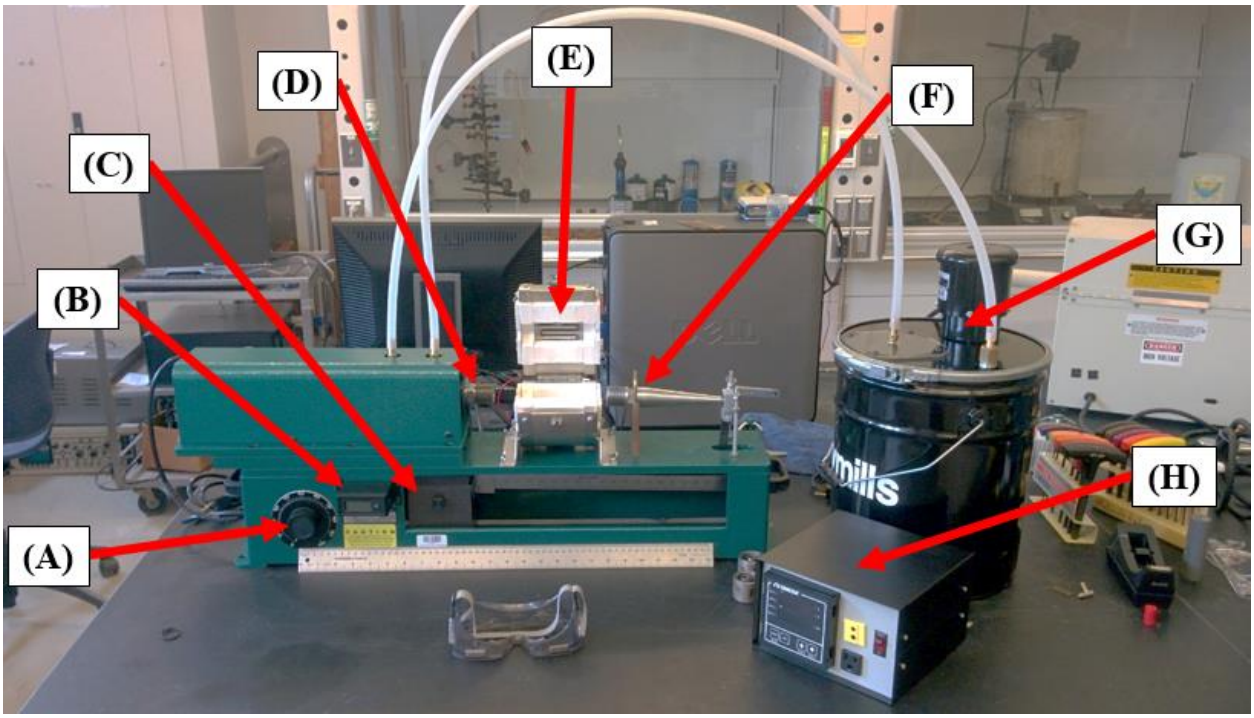

Figure IV.1. Rotating beam fatigue test machine used in the HCF studies **(A)** motor control **(B)** digital counter **(C)** poise weight **(D)** drive collet **(E)** 2100 °F furnace **(F)** loading arm **(G)** spindle cooling pump and reservoir **(H)** furnace controller.

Since the machine has a furnace which adds a 4.5” (114.3 mm) gap between the drive collet **(D)** and load arm **(F)** as compared to the standard machine, a set of collet extenders, shown with the specimen in Figure IV.2 was purchased so a standard 2” (50.8 mm) specimen length can be used.

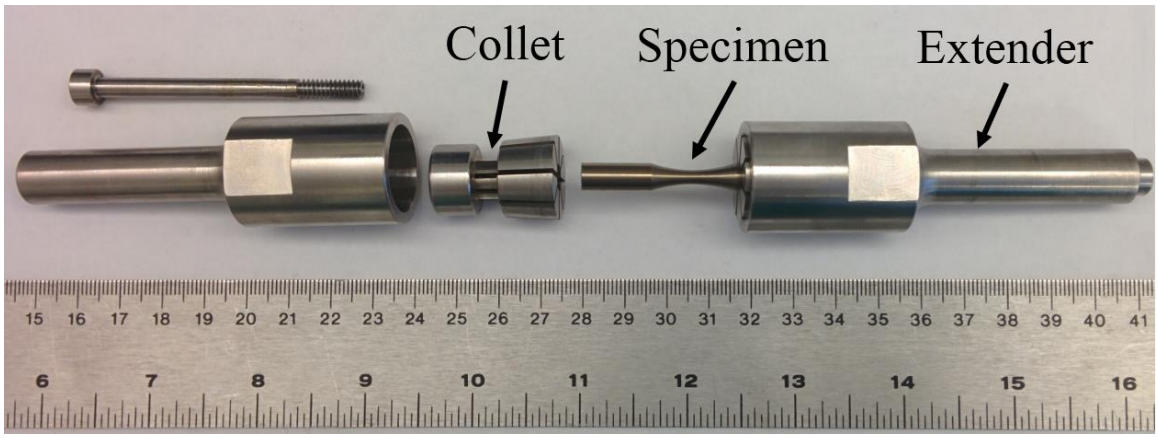

Figure IV.2. HCF specimen with collet extenders.

The test specimen, drawn schematically in Figure IV.3, is inserted into the collet extenders which are then inserted into the drive collet (Figure IV.1 **D**) and load arm collet (Figure IV.1 **F**). When the specimen fails, the load arm collapses and hits a cutoff-switch which turns off the motor, furnace and cooling pump. The digital counter (Figure IV.1 **B)** stops and shows to number of cycles to 100 cycle accuracy.

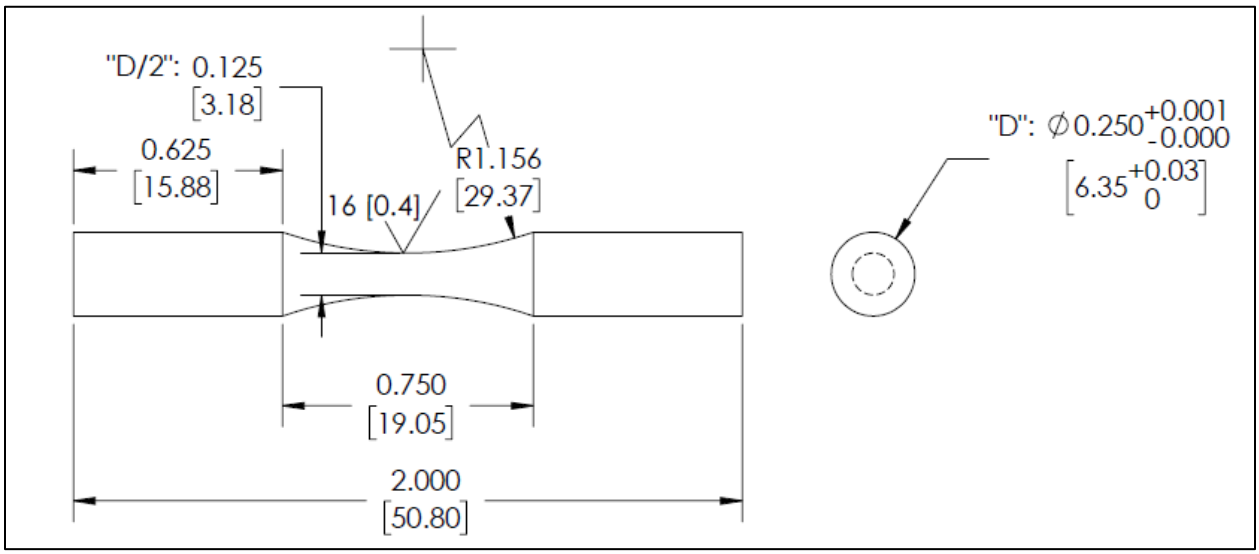

Figure IV.3. HCF specimen - dimensions in inches [mm].

The DMLS samples were printed at Turbocam International in two orientations with respect to build direction (BD): diagonal at 45^{o} (D), and horizontal (H), as shown in Figure IV.4. To compare the high cycle fatigue performance of DMLS and traditionally manufactured alloys, the wrought specimens, also provided by Turbocam, were cut from shaped forgings of Inconel 718. The material was then subjected to heat treatment AMS 5663 as described in Section II.1.

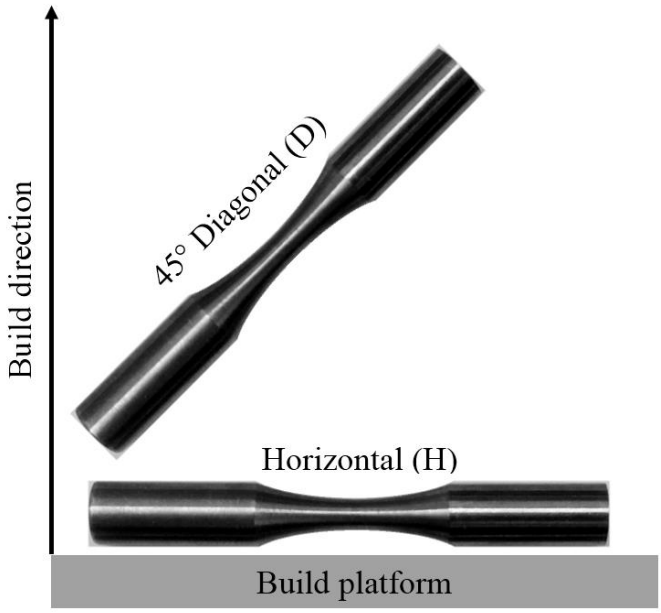

Figure IV.4. Orientation of high cycle fatigue samples with respect to the build direction (BD)

IV.2. Numerical studies to investigate natural frequencies of the high cycle fatigue test setup

The objective of this numerical study is to identify the natural frequencies of the HCF specimen and its fixture in the rotating beam fatigue test to avoid resonance. The results presented in this section were produced in collaboration with a visiting Brazilian undergraduate student, Tulio Francisco, during his summer placement in the UNH Computational Mechanics Lab. Three models have been developed for use in MSC.Marc/Mentat: the isolated specimen, the specimen with the collet extenders fixed at both ends, and the specimen with the extenders as a cantilever beam. The solid models produced in SolidWorks are shown in Figure IV.5.

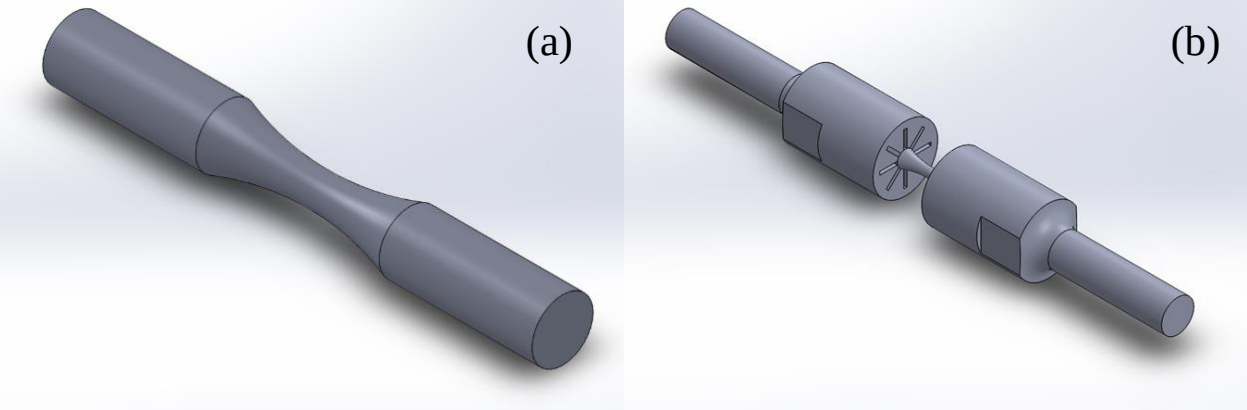

Figure IV.5. 3D SolidWorks models of the HCF specimen and fixture.
(a) HCF specimen. **(b)** HCF specimen in the testing fixture.

These solid models were then exported to MSC.Marc and meshed with linear tetrahedral elements. Mesh information is shown below in Table IV.1. The meshes are shown in Figure IV.6.

Table IV.1. Mesh information for the models analyzed.

Model	Number of Elements	Element Type
Isolated HCF Specimen	1597	Linear Tetrahedral
HCF Specimen in collet extenders	78357	Linear Tetrahedral

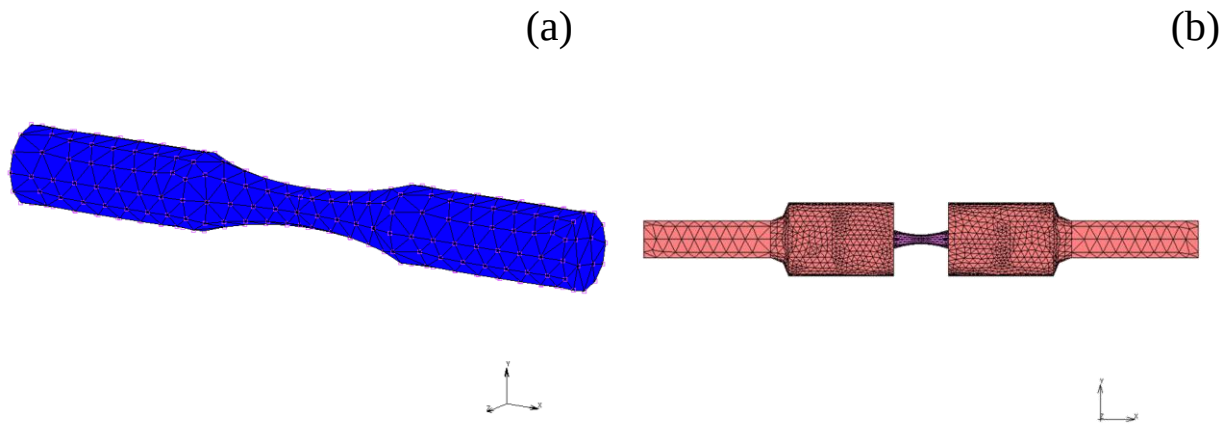

Figure IV.6. 3D tetrahedral meshes for the numerical analyses.
(a) HCF specimen. **(b)** HCF specimen in the testing fixture.

The material properties for Inconel 718 were determined based on the tension tests described in Section III.3. The linear portion of the true stress - true strain curve was fit using the *polyfit* function in MATLAB to find the Young's Modulus (216.5 GPa). The elastic portion of the curve was then removed and true strain was converted to plastic strain using the same process as outlined in Equations (III.5) and (III.6). The true stress- plastic strain curve is shown in Figure IV.7. The material of the extenders is 304 stainless steel. The mechanical and physical properties of both materials are shown in

Table IV.2. Mechanical Properties of Inconel 718 and AISI 304 stainless steel used in the numerical analysis.

Material	Density (kg/m^3)	Young's Modulus	Poisson's Ratio
Inconel 718, DMLS Diagonal	8220	216.5	0.284
AISI 304 stainless steel	8000	200	0.275

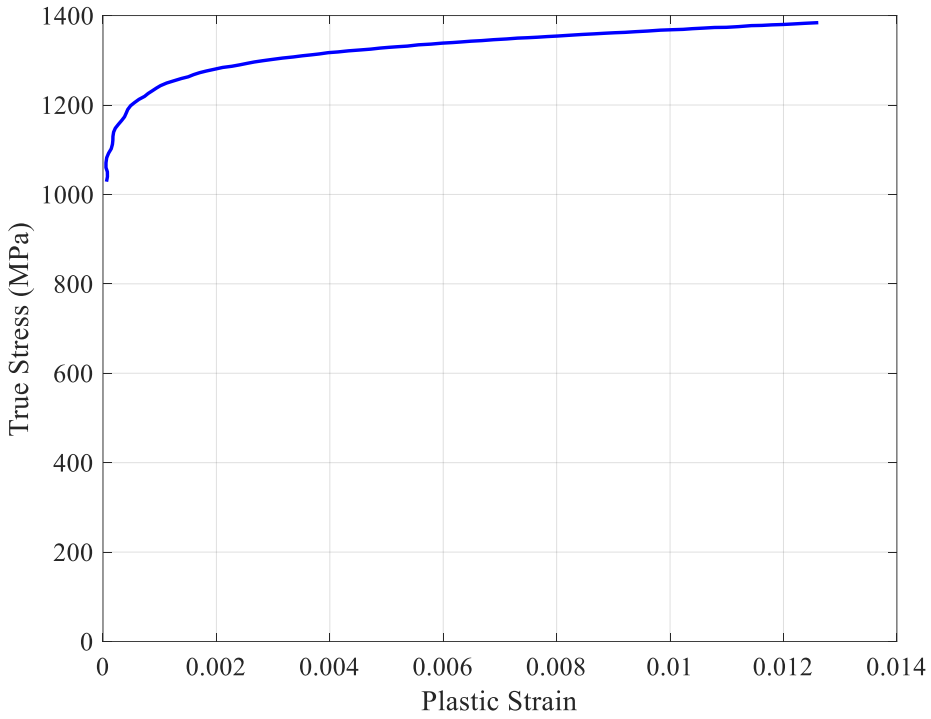

Figure IV.7. The true stress - plastic strain curve for diagonal DMLS Inconel 718.

To find the natural frequency of the isolated specimen in the experimental setup, the grip section of the specimen had a fixed boundary condition on the external surfaces of both sides of the specimen as shown in Figure IV.8.

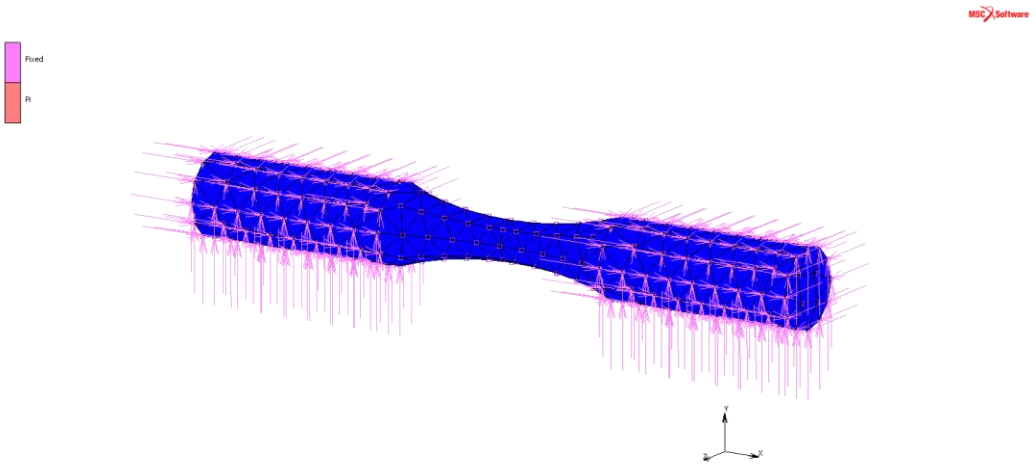

Figure IV.8. HCF isolated specimen boundary conditions.

To find the natural frequency of the specimen and collet extender assembly, the fixed boundary condition was applied to either one or both ends of the collet as shown in Figure IV.9.

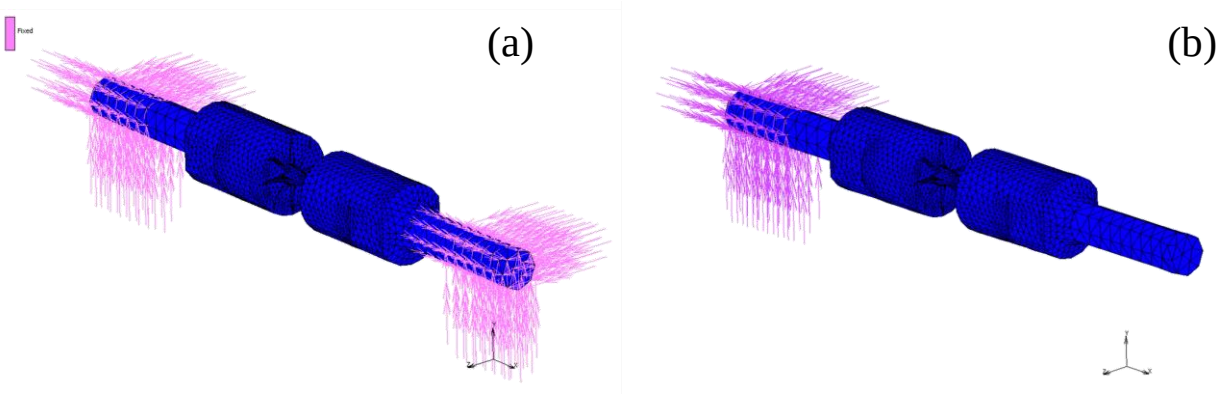

Figure IV.9. Boundary conditions for the full specimen – collet extender assembly analyses. **(a)** Fixed on both ends. **(b)** fixed on one end.

A structural Dynamic Modal loadcase was created to calculate the first three natural frequencies and modes of all models. Figure IV.10 shows the first (fundamental) mode of vibration for each model.

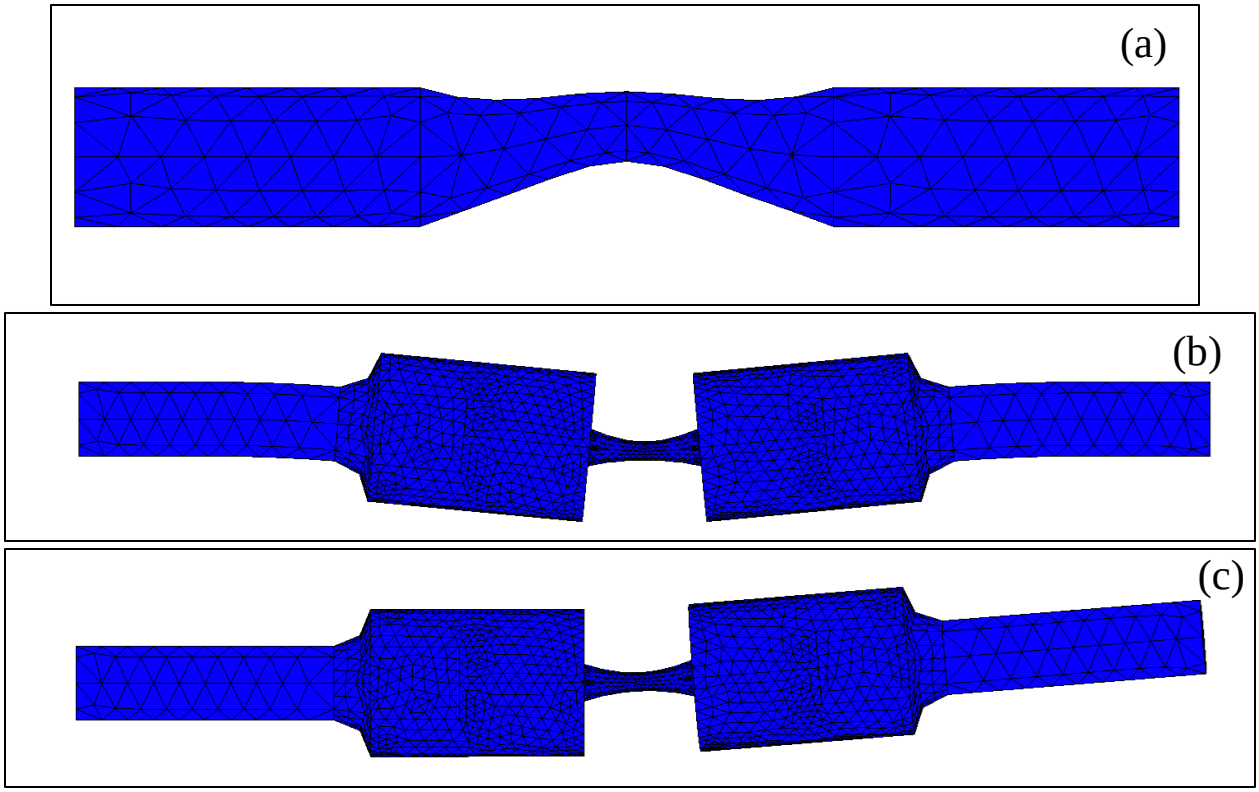

Figure IV.10. Fundamental modes of vibration for the three models.
(a) Isolated specimen. **(b)** Specimen with extenders fixed on both ends. **(c)** Specimen with extenders fixed on one end.

The natural frequencies of all simulations are presented in Table IV.3.

Table IV.3. Summary of the modal analyses on the HCF test setup.

	1st mode [Hz]	2nd mode [Hz]	3rd mode [Hz]
Fixed Specimen	5842	11150	14070
Specimen with the grip fixed on 2 sides	1385	1421	3137
Specimen with the grip - cantilever	89.5	488	915.3

To validate the FEA model, an experiment was performed to observe the resonance in the machine. While applying a stress of 200MPa to the specimen, the rotating beam tester was turned on and the rotating speed then was increased until the resonant vibration of the load arm located

on the right end of the machine was visible. The recorded resonant frequencies from 2 experiment were 86.95Hz and 76.95Hz.

Figure IV.11 Area of the observed vibration in the set up

It is observed that the fundamental frequency predicted by the cantilever beam model of the specimen in the fixture (89.5 Hz) is sufficiently close to the experimental observations. Thus, this model can be utilized for selection of safe frequency regimes for high cycle fatigue testing of various materials.

IV.3. High cycle fatigue testing procedure

Specimens were subjected to cyclic rotating beam fatigue loading at constant stress amplitudes, σ_a, ranging from 200 MPa to 1200 MPa at a frequency of 50 Hz. The bending moment required for a desired stress amplitude is given by the formula

$$M = \frac{\sigma_a \pi d^3}{32} \tag{IV.1}$$

where d is the specimen test section diameter of 0.125” (3.18 mm). Specimens were inserted into the collet extenders and into the drive side collet of the rotating beam tester in such a way as to reduce the rotational runout of the setup as much as possible.

The desired quantities of rotational runout are 0.001” to 0.002” near the drive side collet, 0.004” to 0.006” at the right end of the collet extension setup, and 0.004” to 0.010” at the right end of the load arm as shown in Figure IV.12 [52]. When measuring the experimental runout, it was found that the measured runout exceeded these limits. However, the manual indicates that when running the RBF tester, the setup will often find a new rotational center, and the runout measurement reduces. This will limit the amount of vibration in the setup to the point where the dynamic effects of vibration are negligible [52]. No visible vibration was observed during all experiments.

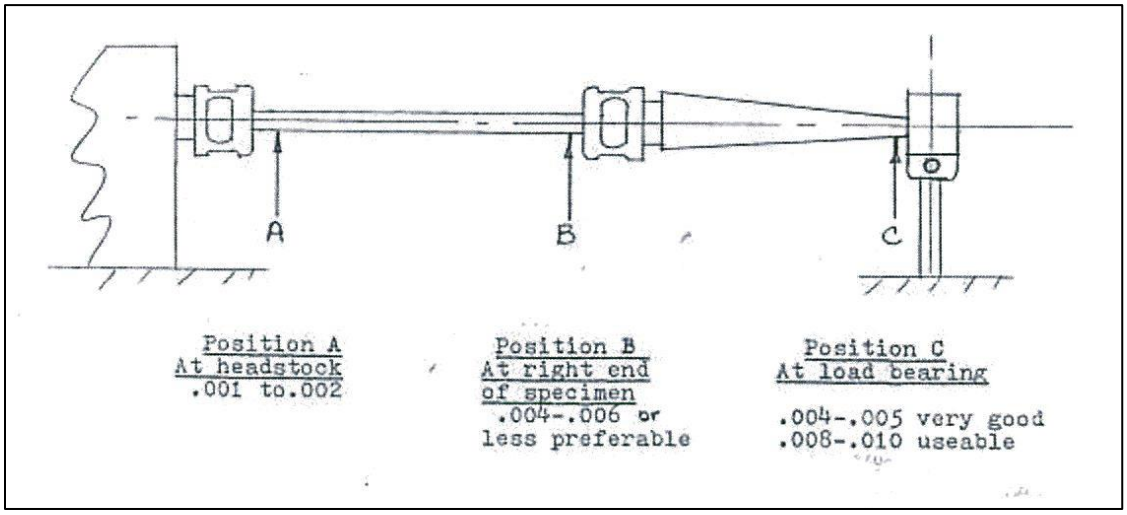

Figure IV.12. Desirable rotational runout for the HCF tests [52].

The motor was brought up to speed while dampening out the load arm with the opposite hand to damp out any resonate frequencies that the system may pass through. The digital counter and a

timer were used to measure the rotational speed of the tester in rotations per minute (RPM), which can be converted to frequency (Hz) by

$$f = \frac{RPM}{60} \tag{IV.2}$$

When the tester was running at the correct speed, the poise weight was positioned to the correct moment and the digital counter was quickly reset to zero to measure the number of cycles under the prescribed load. The tester speed was checked at various points throughout the test and adjusted accordingly, as the load and temperature affected the motor speed.

The number of cycles to failure, N_f, was recorded. Experiments were performed on differently manufactured and treated Inconel specimens at room temperature and 500 °C as shown in Table IV.4.

Table IV.4. High cycle fatigue tests performed for Inconel 718.

DMLS (D, HT*) Stress Amplitude (MPa)		DMLS (H, HT*) Stress Amplitude (MPa)		Wrought (HT* Stress Amplitude (MPa)		DMLS (H, HT*, HIP†) Stress Amplitude (MPa)	
Room Temperature	500 °C	Room Temperature	500 °C	Room Temperature	500 °C	Room Temperature	500 °C
400	600	200	500	450	600		400
500	650	300	550	500	650		425
600	700	350	600	600	700		450
700	800	400	700	700	800		500
800	900	450‡	800	800			550‡
900‡		500	1000	900‡			600
1000		600					700
		700‡					800
		750‡					900
		800					1000
		1000‡					
		1200					

* HT: Heat treated per AMS 5663

† HIP: Hot Isostatic Pressing

‡ Reused specimens that didn't fail at lower stress amplitudes

When performing high temperature tests, *Jet-lube Kopr-Kote*® copper anti-seize compound was applied to all contact surfaces. As in, Kawagoishi et al. (2000), the motor was started 1 hour after the temperature was established in the furnace to ensure that the entire volume of the specimen is heated to the required temperature before initiating cyclic loading [22].

IV.4. Results of high cycle fatigue of Inconel 718

Figure IV.13 presents the $\sigma_a - N_f$ data for all tested samples and loading conditions, arrows indicating that the specimen did not fail and the test was halted at 10^7 cycles. As expected, the general trend is that N_f increases with a decrease in σ_a. However, it can be seen that material manufactured by different processes exhibit certain deviations in fatigue performance, so they are considered separately in consequent discussions.

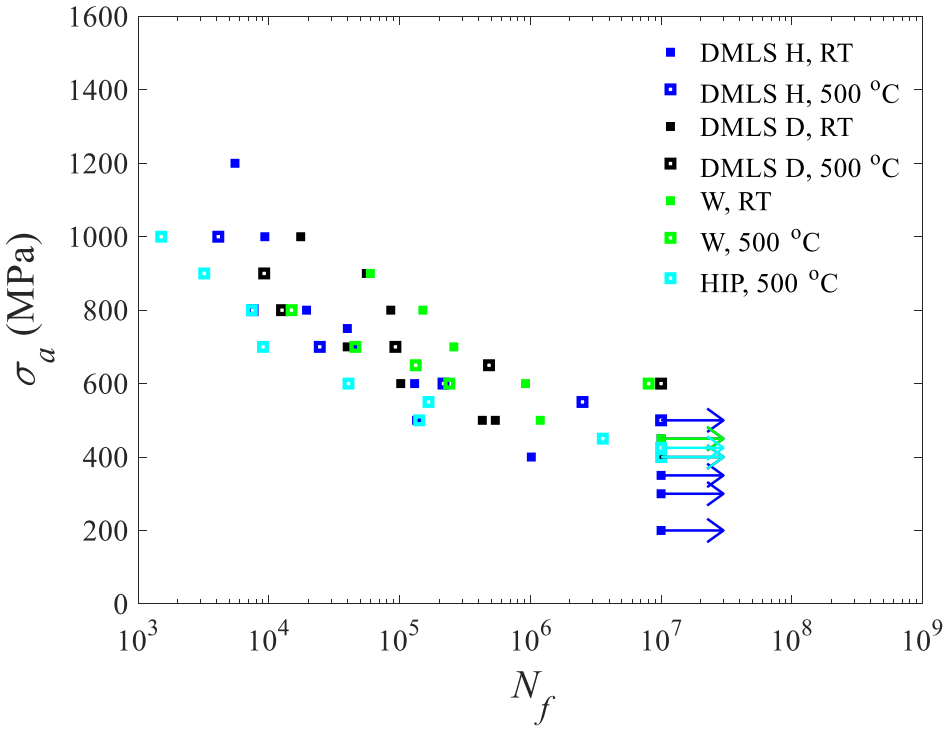

Figure IV.13. σ-N data collected for all tested samples.

Figures IV.14 to IV.17 present the results for differently manufactured materials. The fatigue performance can be modeled by the equation

$$\sigma_a = aN_f^b. \quad \text{(IV.3)}$$

where a and b are the parameters of fit. The model includes all data from only fractured specimens, and the corresponding line of fit is extrapolated to the intersection with the endurance limit of the testing, chosen as 10^7 cycles.

Room temperature data are plotted as solid markers with solid lines and 500°C data are denoted by empty markers with dashed lines. Figure IV.14 a,b compares the accuracy of fit in a linear stress scale against a logarithmic stress scale. The corresponding R^2 values for the goodness of fit are shown in the upper right hand corner of each plot. It can be seen that the logarithmic scaling is a better model for this material.

The coefficients of fit are shown in Table IV.5.

Table IV.5. Parameters of fit for the high cycle fatigue tests.

Material Group	Testing Condition	*a*	*b*
DMLS (D, HT)	RT	6956.0	-0.2011
	500°C	1347.7	-0.0526
DMLS (H, HT)	RT	6705.6	-0.2088
	500°C	1767.1	-0.0834
Wrought (HT)	RT	6750.7	-0.1812
	500°C	1101.2	-0.0416
DMLS (D, HT, HIP)	500°C	2011.9	-0.1070

Note that the number of available wrought Inconel specimens for 500°C tests was not sufficient to exactly determine the fatigue strength corresponding to the chosen endurance limit of 10^7 cycles.

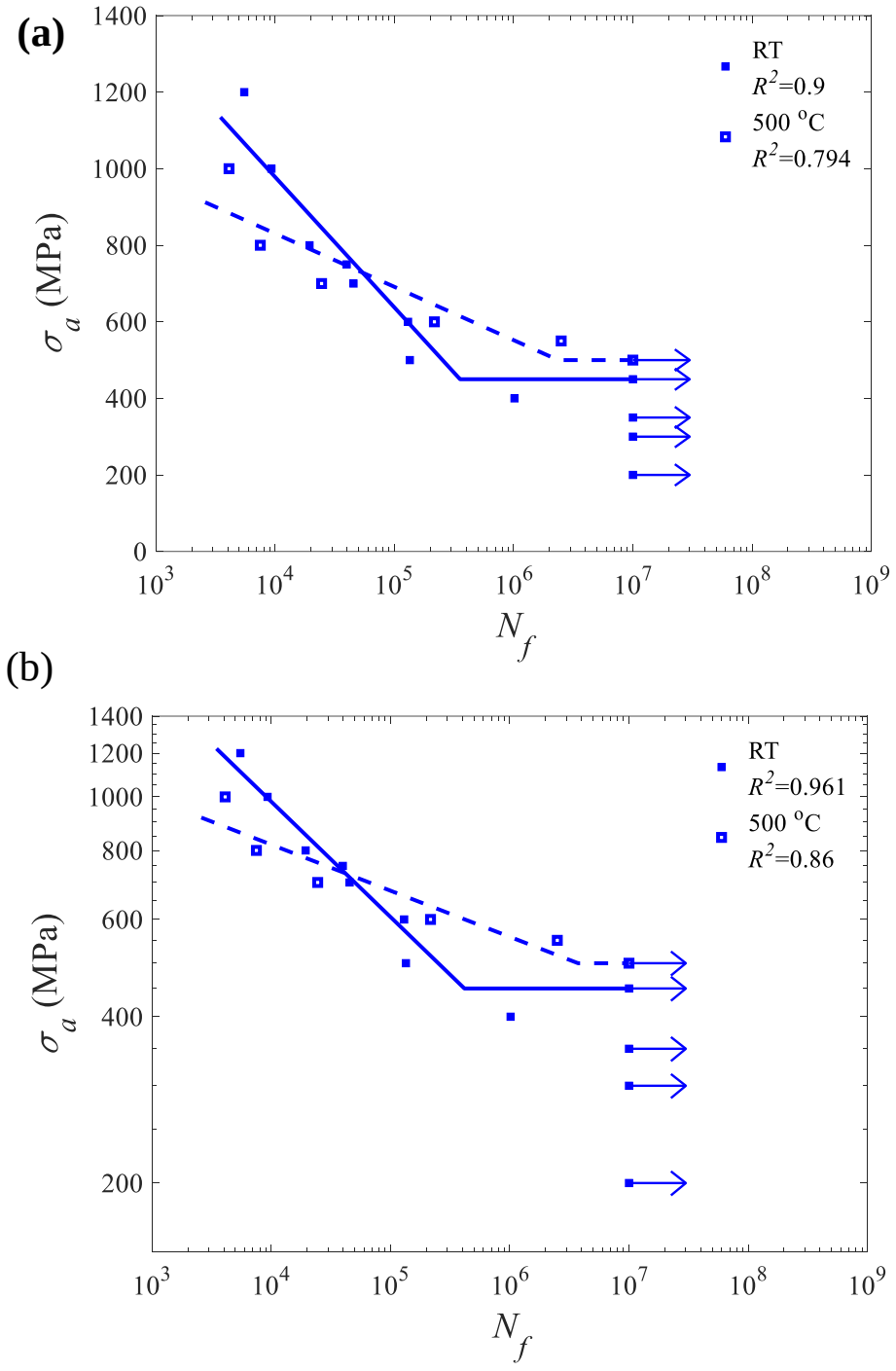

Figure IV.14. Horizontal DMLS Inconel 718 HCF data.
(a) linear stress scaling. **(b)** log stress scaling.

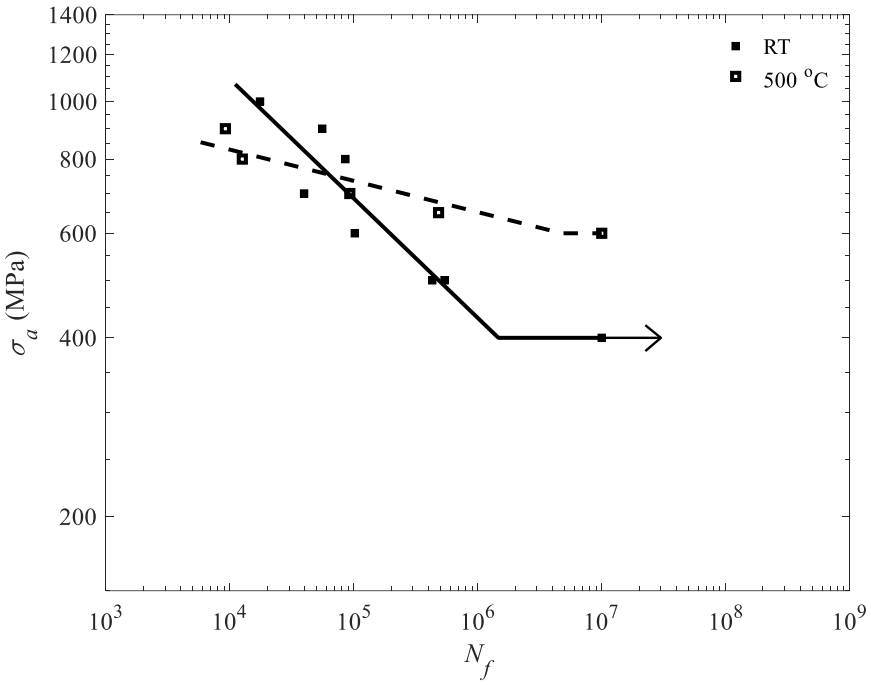

Figure IV.15. Diagonal DMLS Inconel 718 HCF data.

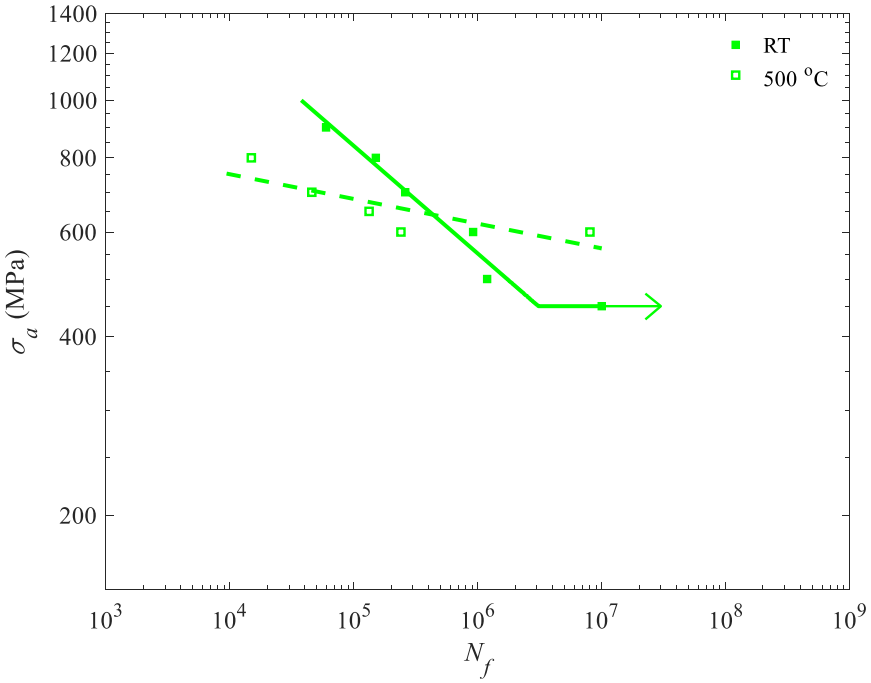

Figure IV.16. Wrought Inconel 718 HCF data.

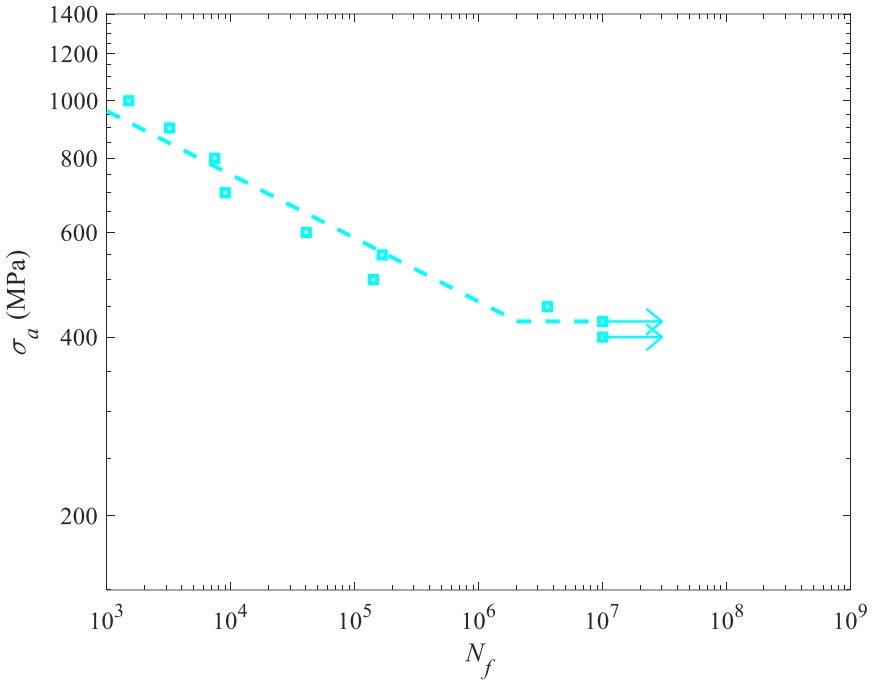

Figure IV.17. HIPed DMLS Inconel 718 HCF data.

For all three materials shown in Figure IV.14 to IV.17, the trend is that at higher temperature, the slope of the σ_a-N_f curve decreases in magnitude. The material has a longer life at 500°C for lower stress amplitudes than the room temperature material. At higher stresses the material at room temperature outperforms the material at 500°C. This trend has also been observed in the literature. Figure IV.18 shows a comparison of the wrought material data to data collected by Kawagoishi et al. (2000) for wrought Inconel 718 using a rotating beam tester at the same temperatures and similar frequency.

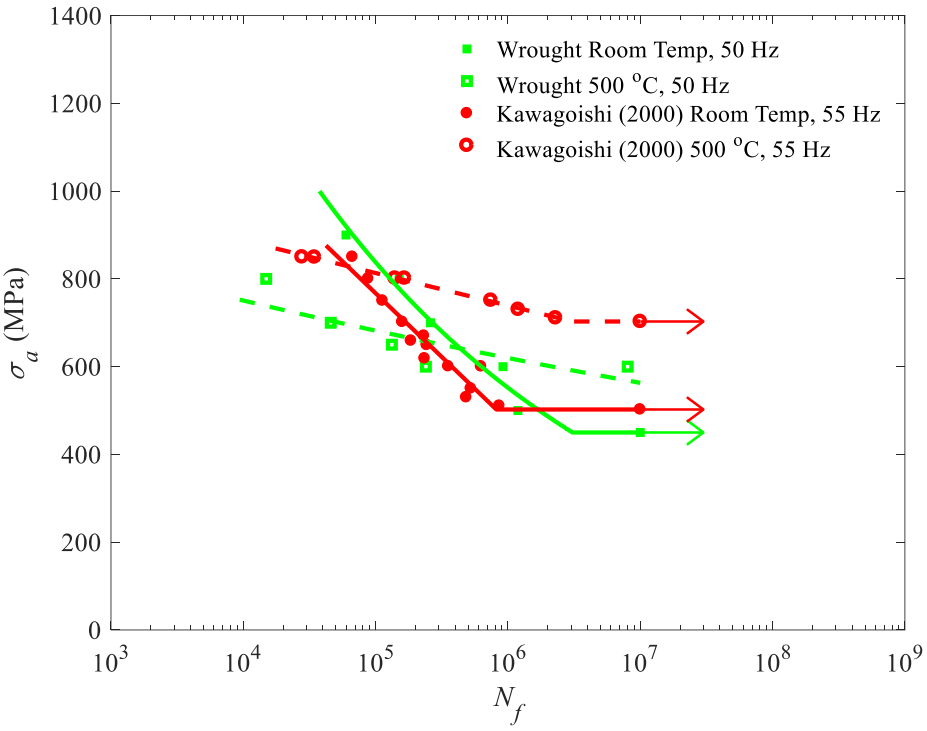

Figure IV.18. Comparison of the wrought material to Kawagoishi et al (2000).

It can be seen that at room temperature, the tested wrought material performed slightly better than the material in the literature, except for the endurance limit which was 450 MPa compared to 500 MPa in the literature. At 500°C, the wrought material demonstrated a significantly better performance in the literature than the tested material. All samples were broken, and no material reached the chosen limit of 10^7 cycles, while an endurance limit was observed at 700 MPa for Kawasgoishi et al. (2000).

A comparison of room temperature tests is shown in Figure IV.19. In general, it can be seen that the wrought material outperforms the DMLS diagonal material followed by the DMLS horizontal material, although the DMLS horizontal and wrought material survived 107 cycles at 450 MPa. There were not enough samples of the DMLS diagonal material to compare at this stress amplitude.

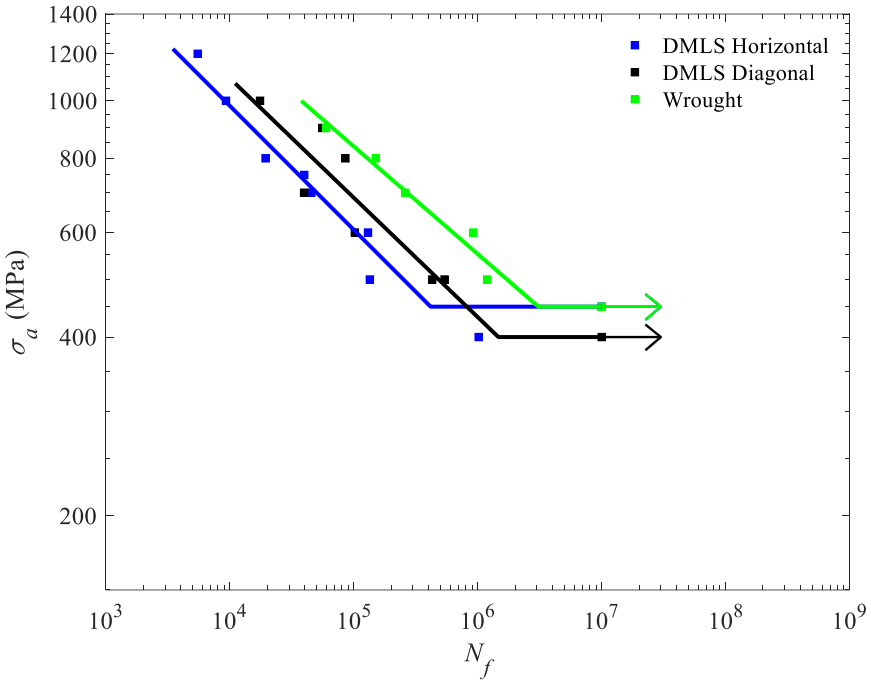

Figure IV.19. Room temperature high cycle fatigue data.

A comparison of 500°C tests is shown in Figure IV.20. At elevated temperature, the wrought and DMLS diagonal materials behave similarly and outperform the DMLS horizontal material followed by the DMLS HIPed material.

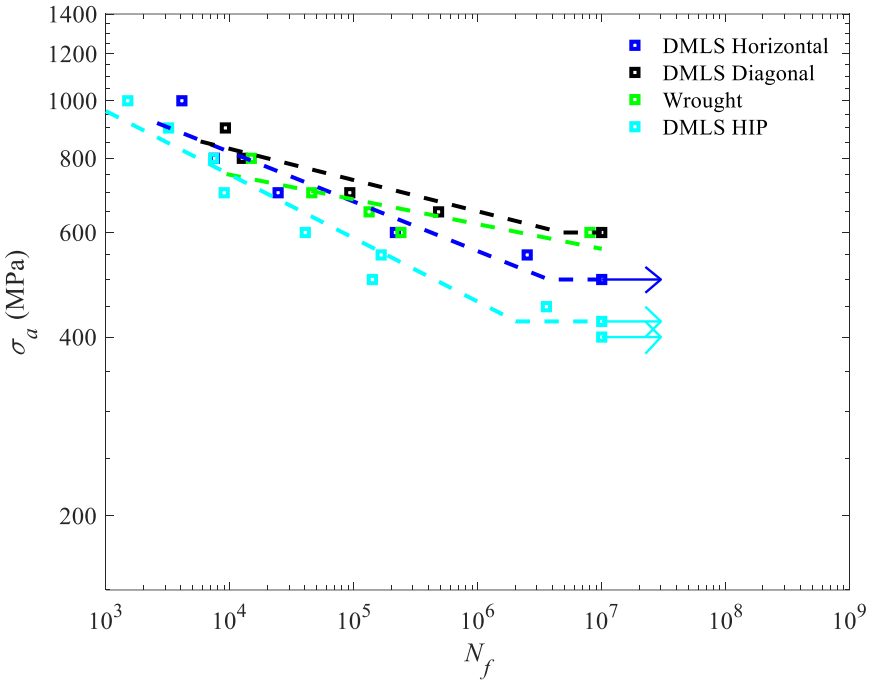

Figure IV.20. 500°C high cycle fatigue data.

From these tests, it can be concluded that high cycle fatigue performance is sensitive to the manufacturing technique and post-manufacturing treatments. In particular, the HIP treatment noticeably reduces the fatigue performance of the DMLS Inconel 718in the high cycle regime as seen in the low cycle regime.

It can be seen that the trend in fatigue performance in the high cycle fatigue regime is different than that of the low cycle fatigue regime, where the strongest material was DMLS diagonal, followed by DMLS horizontal, wrought and HIPed as shown in Figure III.15. In HCF the wrought material performed the best, followed by DMLS diagonal, DMLS horizontal and HIPed.

IV.5. Scanning electron microscopy of select high cycle fatigue sample facture surfaces

Figure IV.21 shows the fracture surfaces of different specimens under different testing conditions:

- DMLS diagonal, room temperature, 500 & 1000 MPa
- DMLS diagonal, 500°C, 900 MPa
- DMLS horizontal, room temperature, 400 MPa
- DMLS horizontal, 500°C, 550 MPa
- Wrought, room temperature, 700 MPa
- Wrought, 500°C, 600 MPa
- DMLS horizontal & HIPed, 500°C: 600 & 900 MPa

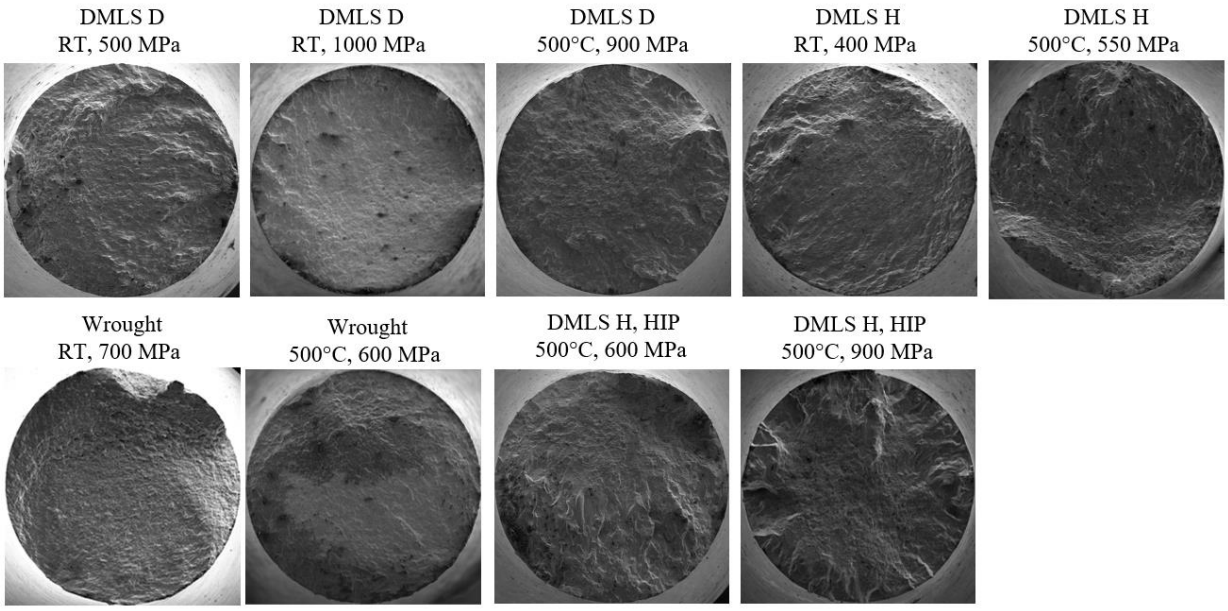

Figure IV.21. Fracture surfaces of select high cycle fatigue specimens.

Looking at the DMLS diagonal specimen cycled at 500 MPa at room temperature and comparing to the DMLS horizontal specimen cycled at 400 MPa at room temperature, the fracture surfaces appear very similar, with a large ductile failure surface appearing in the center of the specimen and brittle failure towards the outer surface of the specimen. The wrought material

appears to have a smaller brittle fracture zone around the surface of the specimen, while the HIP material has a much larger brittle fracture zone when compared with the DMLS material.

This ductile/brittle failure pattern is shown more clearly in Figure IV.22, with the finely dimpled zone being the ductile failure area. The areas outlined in red are presumed to be crack initiation sites on the surface of the specimen.

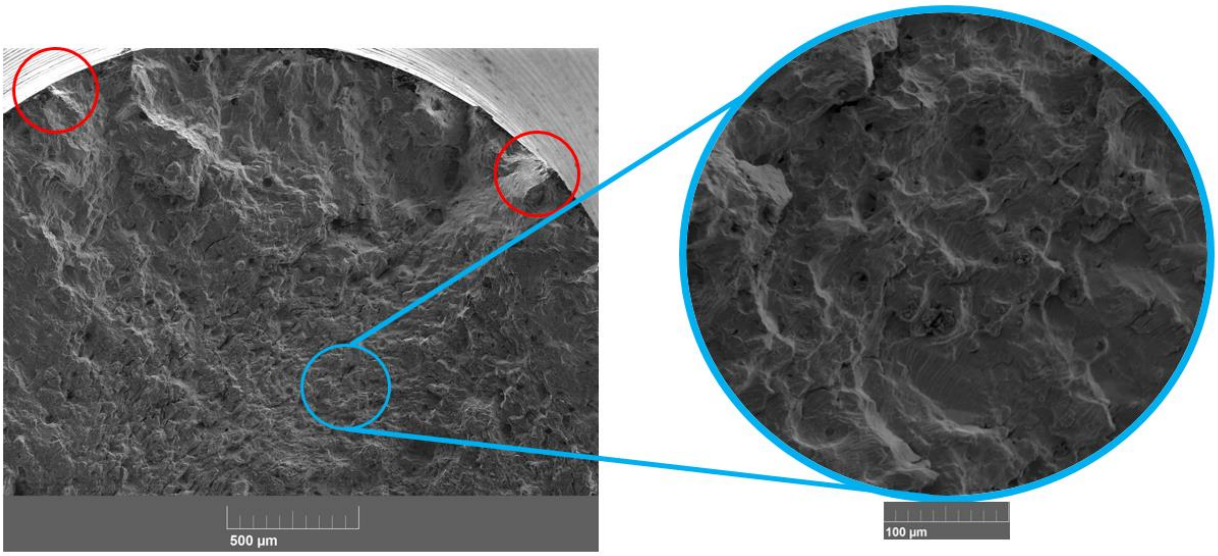

Figure IV.22. 245X magnification of the DMLS D specimen fracture surface, cycled at 900 MPa at 500°C. The inset shows a 1340X magnification of the ductile failure zone.

It appears the mechanism behind these features is the distribution of stress on the specimen. The largest stress occurs on the surface of the specimen, and linearly diminishes going towards the center of the specimen, where the stress is theoretically zero. In fatigue, cracks initiate from the surface and occasionally internal defects. The higher stress on the surface of the specimen promotes brittle behavior while the lower stress in the center of the specimen slows down the propagation of cracks, results in ductile failure.

The HCF performance of Inconel 718 appears to be correlated to the proportion of ductile to brittle failure area on the fracture surface of the specimen. The wrought material showed the largest

area of ductile fracture, with small outer portions exhibiting brittle fracture. The pattern results in better performance when compared to the DMLS heat treated material and DMLS heat treated and HIPed material, which show increasing area of brittle fracture on the fracture surfaces as evidenced in Figures IV.19 and IV.20.

V. LOW CYCLE FATIGUE OF A FIBER-REINFORCED VINYLESTER COMPOSITE

In this chapter, the low cycle fatigue (LCF) behavior of a fiberglass reinforced vinylester composite is presented. Rectangular coupon specimens were manufactured by HALO Maritime Defense Systems according to ASTM D3039. Tension-tension stress-controlled fatigue experiments were conducted for maximum stresses ranging from 250 MPa to 350 MPa to investigate how the stress magnitude relates to the number of cycles to failure. A final report was submitted to HALO in February 2016.

V.1. Fiber-reinforced vinylester composite material processing and low cycle fatigue specimen design

The investigated material is a pultruded fiberglass-reinforced vinylester composite manufactured by Bedford Reinforced Plastics (bedfordreinforced.com). It consists of a unidirectional fiberglass layer between two multidirectional fiberglass mats. The fiberglass layers are pulled through bath of vinylester resin and catalyst to aid the cuing process. A surface veil is added to improve the appearance of the material and the material is then pulled through a heated pultrusion die where the resin cures [53].

Specimens were prepared by HALO in accordance with ASTM D3039 [54]. They were 1.25 in. (31.75 mm) wide, 0.125 in. (3.18 mm) thick. 0.125 in. thick tabs were glued to the grip section using PLIOGRIP® 7779 Urethane Adhesive as shown in Figure V.1. The loading direction is parallel to the direction of the pultruded fibers. These specimens were stored and tested at room temperature (25-30°C).

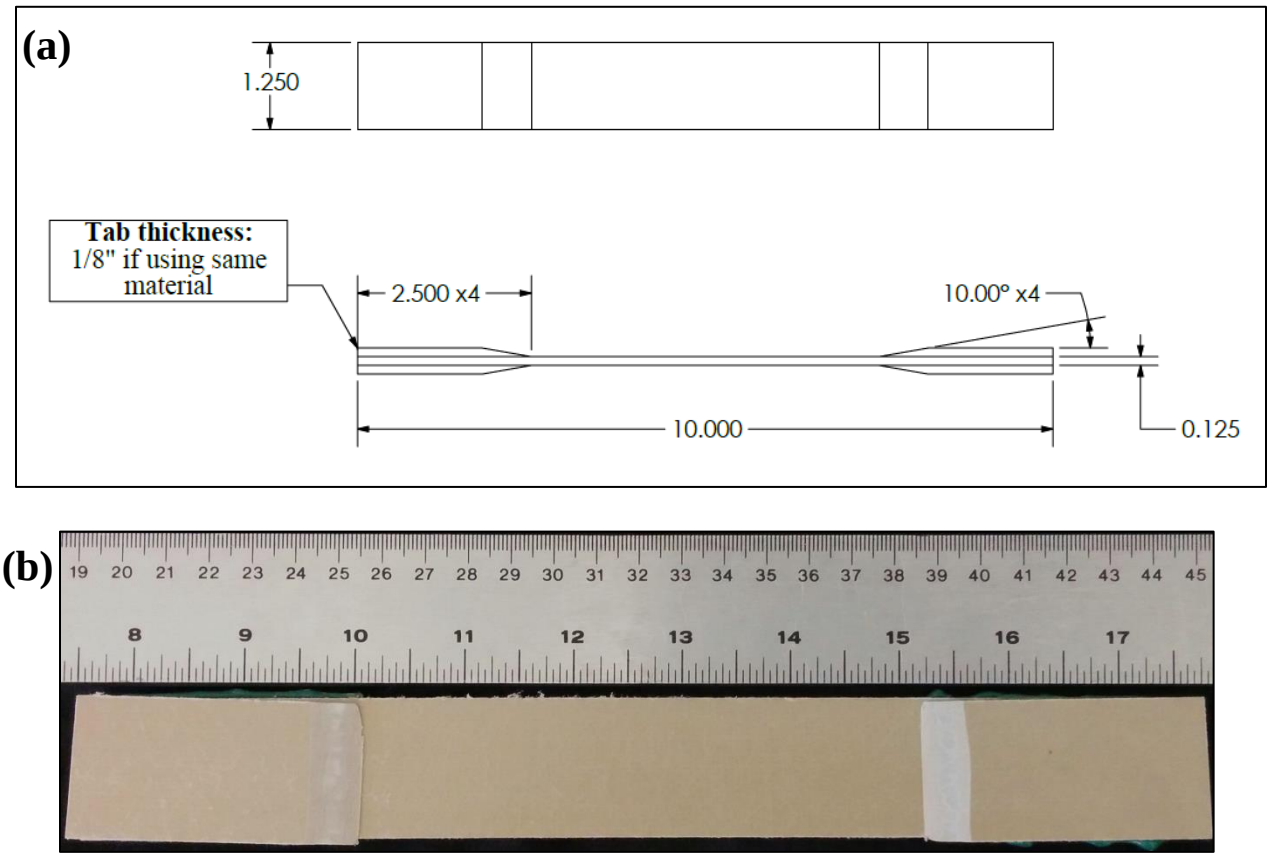

Figure V.1. Vinylester low cycle fatigue specimen: (a) drawing and dimensions in inches (b) the actual specimen manufactured by HALO.

Material properties provided by Bedford Reinforced Plastics are given in Table V.1 [53].

Table V.1. Static tension material properties for 1/8" vinylester plate.

Ultimate Tensile Stress (σ_{UTS}), Lengthwise	137.9 MPa
Tensile Modulus (E), Lengthwise	12.4 GPa
Poisson's Ratio (ν)	0.31

V.2. Monotonic tension tests of a fiber reinforced vinylester composite

Before beginning fatigue experiments, tensile testing was performed to obtain the reference static tensile properties of the material and compare them with the manufacturer's data. Four

tension experiments were conducted using the MTS Landmark 270 load frame. Force data was collected using a MTS model 661.22H-01 250kN load cell which has a maximum output error of 0.35% in compression and 0.09% in tension. Axial displacement of the specimen was measured using a MTS model 634.12E-24 2" extensometer calibrated to within 1% accuracy as outlined in Chapter III.1.

Forces and displacements were then converted into engineering stresses and strains according to the formulae III.1 and III.2 found in section III.1.

The specimens were pulled in tension to failure under displacement control with a strain rate of approximately $2.3 \times 10^{-4}\ s^{-1}$. The stress strain curves are shown in Figure V.2.

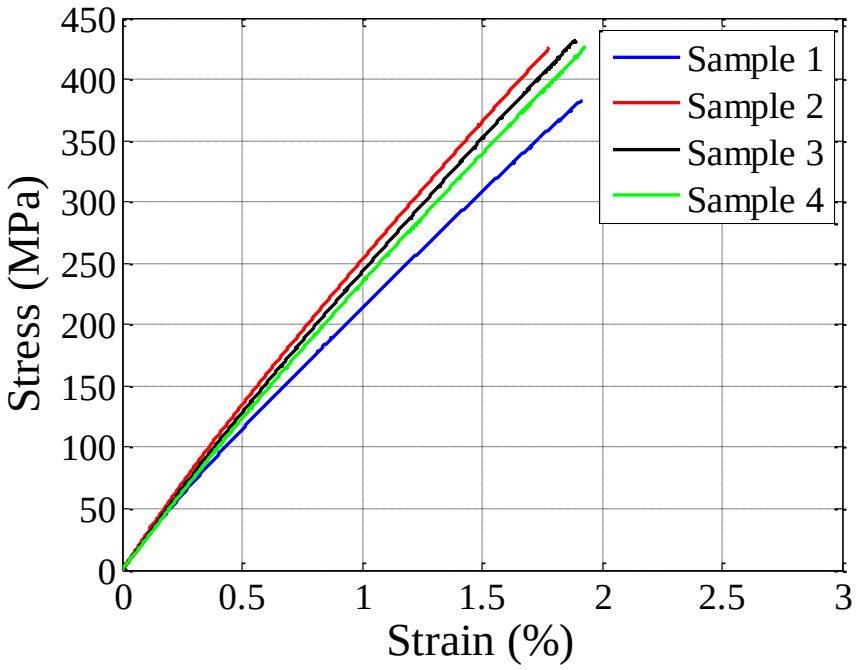

Figure V.2. Engineering stress –strain response of four vinylester composite samples.

Material properties taken from the tests are shown in Table V.2. The average ultimate tensile stress is 427.69 MPa with a 1.42% variation. The average tensile modulus is 22.91 GPa with a 7.94% variation. Note that Sample 1 was excluded from the average value as it had a much lower

modulus and ultimate stress than the other three samples. It was assumed that it was an outlier with some initial defect influencing the material behavior.

Table V.2. Static tensile material properties of vinylester composite.

	Tensile Modulus (GPa)	Ultimate Stress (MPa)	Ultimate Strain (%)
Sample 1	19.97	382.75	1.92
Sample 2	23.87	425.49	1.78
Sample 3	22.81	431.56	1.89
Sample 4	22.05	426.03	1.93
Average	22.91	427.69	1.87
Standard Deviation	0.914	3.356	0.077
BRP* Specifications	12.4	137.9	--

*Bedford Reinforced Plastics

It is observed that there is a significant difference between the manufacturer's specifications and our measurements: 84.8% for tensile modulus, 210% for the ultimate strength. Even if a different criterion for failure is used (observation of micro-damage vs. macroscopic delamination) it still doesn't explain the lower value of the elastic modulus reported by the manufacturer. Overall, it appears that using the manufacturer's values of the tensile modulus and ultimate stress will constitute a conservative approach to design.

V.3. Low cycle fatigue of a fiber reinforced vinylester composite testing procedure

Tension-tension low cycle fatigue experiments were conducted according to ASTM D3479 [55]. The same MTS servohydraulic machine was used as for the static tension experiments. The specimens were pulled in tension under displacement control up to certain maximum engineering stress and unloaded to zero load in a triangular waveform until specimen failure. The stress waveform generated for a sample loaded to 350 MPa is shown in Figure V.3. Note that there is

some non-linearity of the stresses in the first loading cycle, as the machine is run under displacement control.

The displacement rate was set to 0.5 mm/s, which corresponded to strain rates of about $2.6 \times 10^{-3}\ s^{-1}$ to $2.8 \times 10^{-3}\ s^{-1}$ and frequencies ranging from 0.082 Hz to 0.137 Hz depending on the amplitude of stress. In a paper published by Demers (1998) [56], frequencies of fatigue load under 4 or 5 Hz have been reported to produce negligible internal heating in glass fiber reinforced polymeric composites. This eliminated the requirement to run temperature controlled experiments.

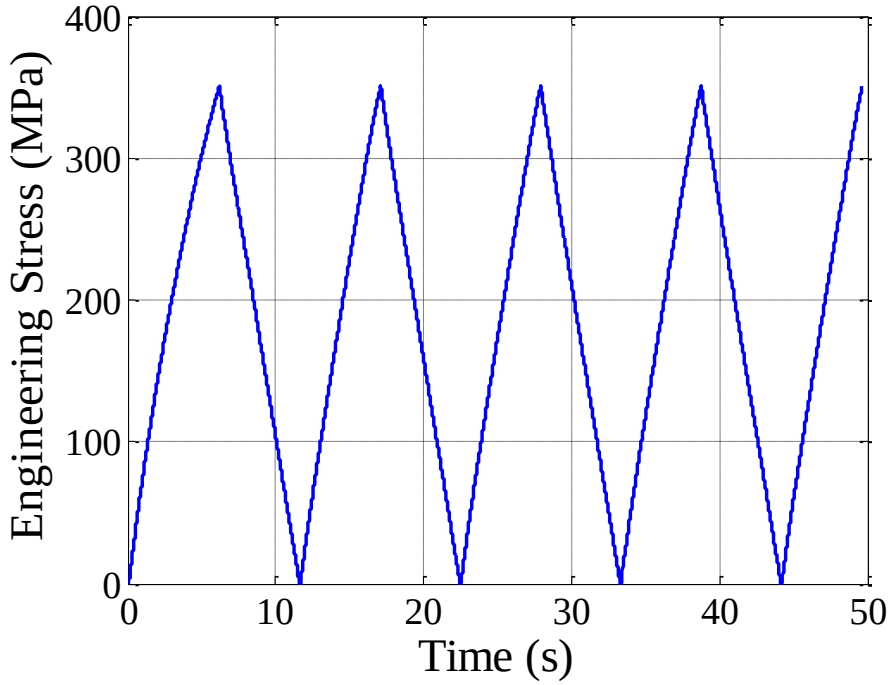

Figure V.3. Stress waveform for a vinylester low cycle fatigue sample loaded to 350 MPa.

V.4. Results and discussion of low cycle fatigue of a fiber reinforced vinylester composite

Table V.3 summarizes the results of the low cycle fatigue experiments completed. The experiments performed are organized by the maximum stress and its percentage of the ultimate

stress taken from the static tension experiments. The maximum stress varied from 250 MPa (59% of the materials ultimate stress) to 350 MPa (82% of the ultimate stress) in 50 MPa increments.

Three specimens were tested at each stress level to investigate the repeatability of the experiments, with the exception of the 325 MPa stress level, where only two experiments were conducted. The observed number of cycles to failure (N_f) is provided for each test, as well as the average N_f for each loading amplitude.

Table V.3. Low cycle fatigue experiments completed on a fiberglass vinylester composite. The second column expresses the maximum stress as a percentage of σ_{UTS} = 427.7 MPa.

Max Stress	% σ_{UTS}	N_f			
MPa	%	01	02	03	Average
250	59	1731	2131	1026	1629
275	64	378	1382	1782	1181
300	70	396	689	278	454
325	76	238	254	--	246
350	82	44	62	173	93

As expected, the overall trend shows that as you increase the stress amplitude, the number of cycles to failure decreases, with some overlap, as there is quite a large variation for each stress amplitude.

It is important to note that the major mode of failure for the composite material was delamination. The onset of this failure could be observed both visually, as seen in Figure V.4, and when looking at the apparent stiffness of the material over the life the specimen, where apparent stiffness is defined as

$$E_{app} = \frac{\sigma_{max}}{\varepsilon_{max}} \tag{V.1}$$

where σ_{max} is the maximum stress and ε_{max} is the maximum strain during each loading cycle.

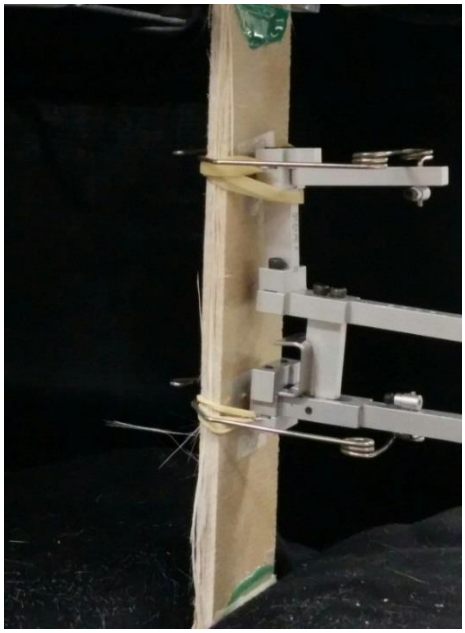

Figure V.4. Observable delamination of the vinylester specimen at failure.

As an example, a graph of the apparent stiffness of a specimen loaded to 250 MPa is shown in Figure V.5. Failure was defined as when the change in stiffness was greater than 0.5% over a period of 5 cycles. The failure of the considered specimen occurred after 1731 cycles.

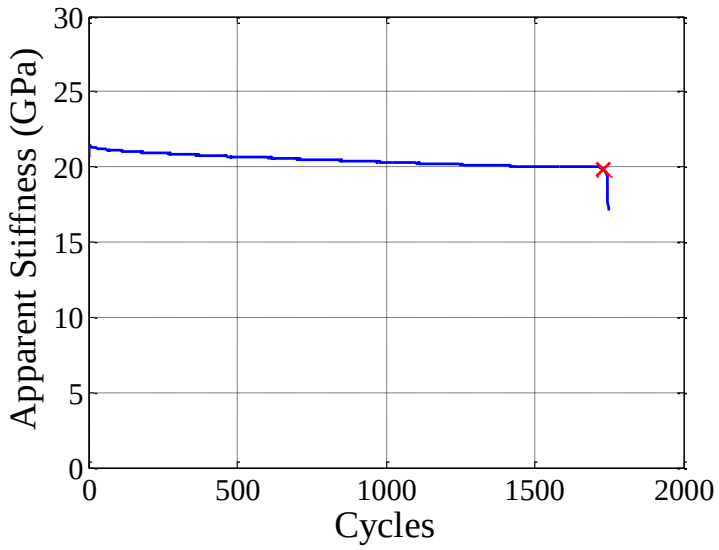

Figure V.5. The apparent stiffness of a specimen cycled to 250 MPa; the failure occurred after 1731 cycles.

Figure V.6 shows a case where the specimen, cycled to 275 MPa, appears to have an increase in apparent stiffness at the end of its life. This is also an indicator of delamination, as the extensometer may be attached to a layer that has delaminated, and therefore has invalid measurements of the specimen deformation.

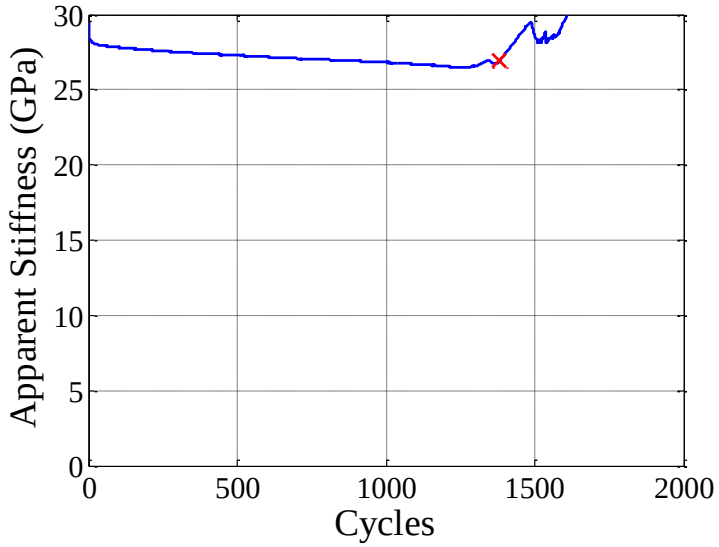

Figure V.6. The apparent stiffness of a specimen cycled to 275 MPa; the failure occurred after 1382 cycles.

Figures V.7 and V.8 show the stress-strain response for the first, second, 50% life and 90% life cycles. For each experiment, there was some irreversible strain accumulated after the unloading in the first cycle due to the non-linear stress-strain response of the material. Afterwards, the stress-strain response remains fairly linear and doesn't change much between 25% and 90% of life.

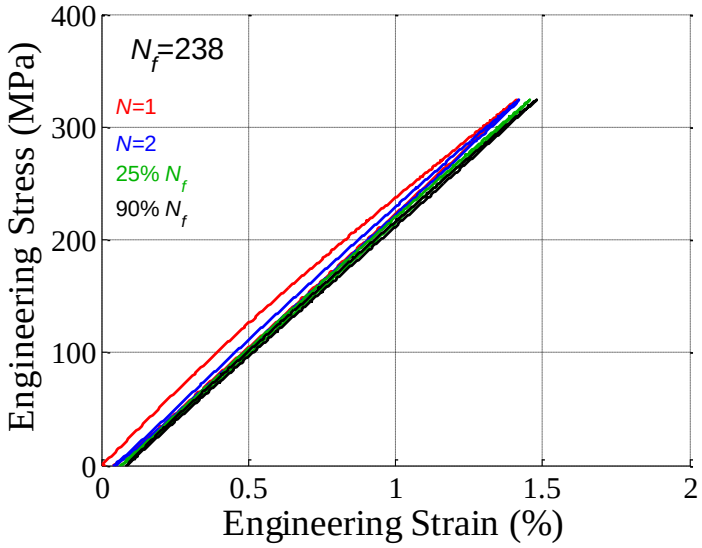

Figure V.7. Stress-strain response for the first, second, 50% life and 90% life cycles of a specimen cycled to 325 MPa; the specimen failed after 238 cycles.

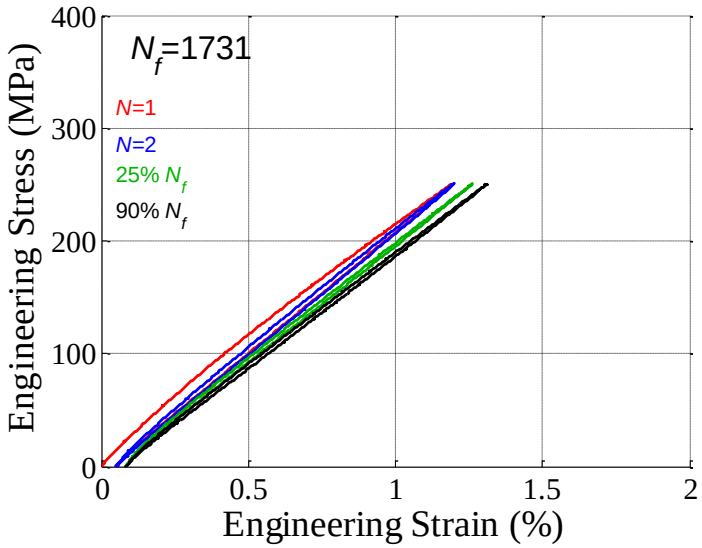

Figure V.8. Stress-strain response for the first, second, 50% life and 90% life cycles of a specimen cycled to 250 MPa; the specimen failed after 1731 cycles.

Figure V.9 compares the degradation of stiffness for different stress amplitudes. It can be seen that there is slight softening of the material after the first few cycles until failure for all stress amplitudes.

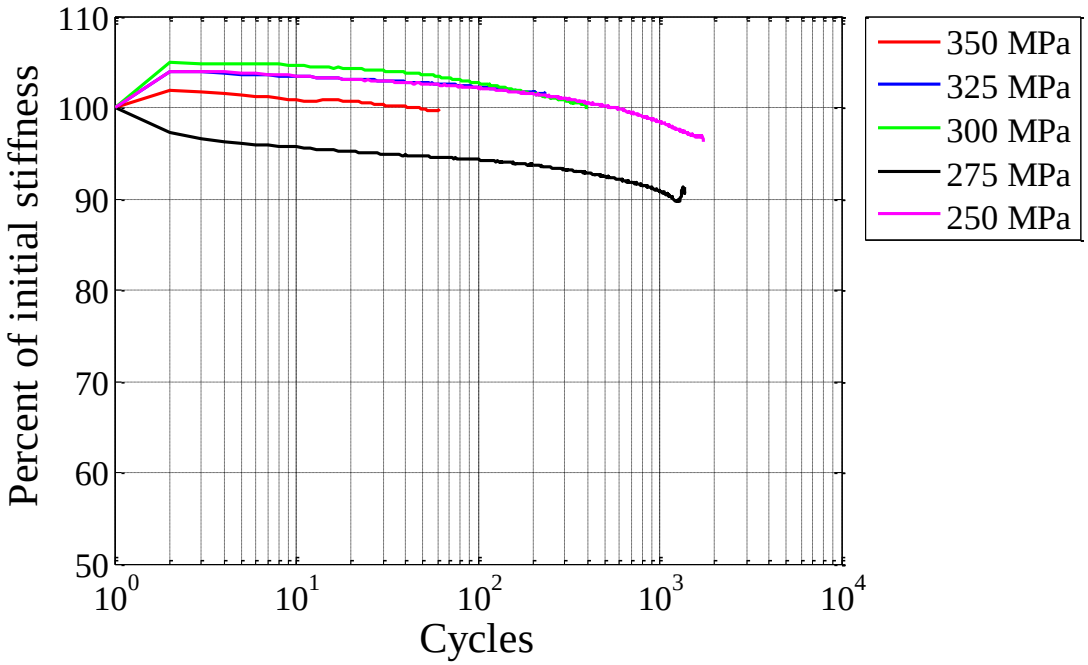

Figure V.9. Degradation of stiffness of specimens over the life of the specimen.

Figure V.10 shows the stress amplitude-life plot for the collected data. It can be seen that there is quite a large variation in the number of cycles to failure for each stress amplitude. This may be expected for a composite material, as there is less consistency in composite material properties as compared to metal alloys [56].

The data presented in Table V.3 is fit with the S-N fatigue curve

$$S = A + B \cdot \log(N_f) \tag{V.2}$$

where S is the maximum stress as a percent of ultimate stress and A & B are the fit parameters, which are an intercept and a slope when plotted in a log scale [57].

The linear fit for the reported experiments results is

$$S = 108.96 - 6.468 \cdot \log(N_f) \tag{V.3}$$

with an R^2 value of 0.825. Note that the value of the intercept is expected to be close to $A = 100\%$ as this would correspond to failure of the material during the first cycle when $\sigma_{max} = \sigma_{UTS}$. The obtained value of A=108.96% is within the variations observed by other researchers [56, 58].

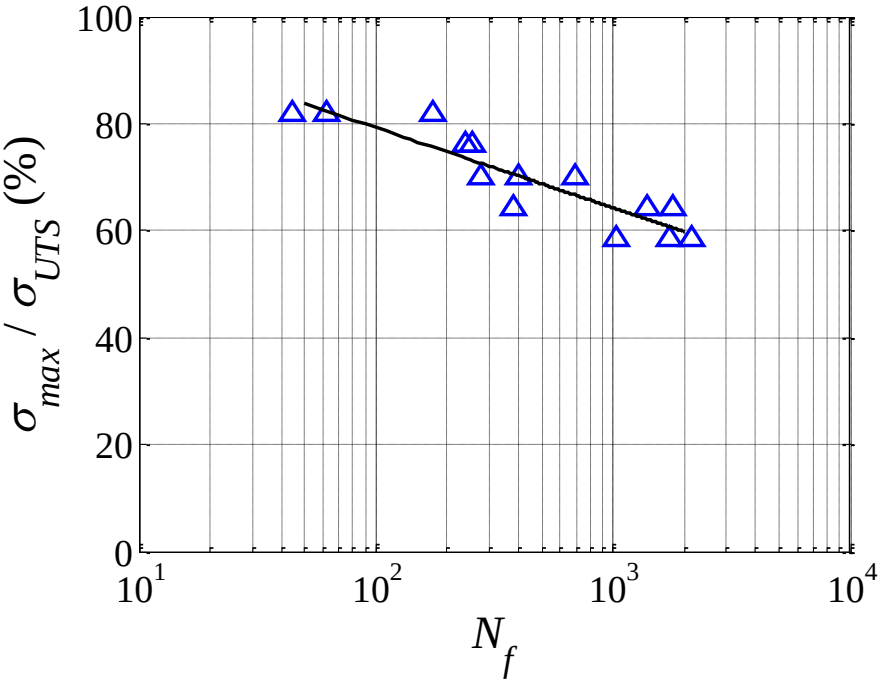

Figure V.10. Stress-life curve data and fit; the fit has an R^2 value of 0.825.

The lower bound S-N curve for a group of fiberglass reinforced composite materials as reported by Demers (1998) [56] is

$$S = 79 - 7.8 \cdot \log(N_f) \qquad \text{(V.4)}$$

This lower bound represents a large variety of data under different testing conditions and presents a very conservative design curve for fatigue of fiberglass reinforced composites when compared to the tested samples.

From the static tension tests performed, it is apparent that the manufacturer's specifications under predict both the stiffness and strength of the vinylester composite material. It would be reasonable to use these values in design for a conservative approach.

During fatigue loading, there is an insignificant reduction on apparent stiffness. This means that the apparent stiffness cannot be used to accurately predict remaining life. The high variability in cycles to failure for the same loading amplitude, typical for composite materials, creates a large uncertainty in the material's life prediction.

VI. CONCLUSIONS

The microstructural features of a direct metal laser sintered Inconel 718 were characterized using electron backscattered diffraction and compared to a traditionally manufactured wrought Inconel 718. Images were taken in different directions with respect to build direction. The specimens underwent a heat treatment cycle AMS 5663, in addition to a group of specimens undergoing a hot isostatic pressing (HIP) treatment. This HIP treatment was enough to trigger recrystallization in the material and produced a much larger grain size compared to the double-aged DMLS material.

The DMLS followed by double aging processed material shows elongated grain structure in the build direction with an approximate aspect ratio of four and a small content of annealing twins. The DMLS followed by double aging and HIPing processed samples show equiaxed grain structure and a high content of annealing twins. Wrought and double-aged samples show the typical equiaxed grain structure with some fraction of the twin boundaries, which is much less than in the HIPed material. The grain size is also smaller than in the HIPed material.

DMLS Inconel 718 low cycle fatigue specimens were manufactured in accordance with ASTM E606 by Turbocam International in a diagonal and horizontal orientation with respect to the loading direction and underwent an AMS 5663 heat treatment. A group of specimens also underwent the HIP treatment. Samples were cycled under strain controlled axial low cycle fatigue in strain amplitudes ranging from 0.6% to 1.4% engineering strain with a mean strain of 0.5% using a 250kN *MTS Landmark 270* servohydraulic testing system. A set of wrought Inconel 718 samples in the same condition was also tested, and the results compared against the results for the DMLS materials.

As expected, the number of cycles to failure decreases with increase of the strain amplitude for each material category. Each material also shows cyclic hardening the first serval cycles of testing, followed by a steady period of softening without stabilization until failure. The failure of the DMLS samples is always abrupt, while the wrought material exhibits a more gradual failure. A mean stress is present in each of the tests, and for larger strain amplitudes, is almost immediately accommodated by plastic deformation and approaches zero with continuation of the test. Moreover, it becomes compressive for the wrought material, which is highly desirable for extending the fatigue life. A reduction in elastic properties is also seen during the life of the material, and can be correlated to increase in strain amplitude. It is assumed that the accumulation of residual stresses in the material accounts for this reduction in elastic modulus.

The DMLS material, which has a higher strength, also has a longer LCF life than the wrought material for low strain amplitudes. The diagonal DMLS material has a longer life than the horizontal DMLS material since it has a slightly higher strength due to grain structure. As the strain amplitudes increase, the plastic deformation mechanisms and the underlying ductility becomes more important and the ductile wrought material exhibits better fatigue performances. The shorter life of the HIPed material for the same strain amplitude can be explained by large content of annealing twins in its microstructure.

DMLS Inconel 718 high cycle fatigue specimens were manufactured by Turbocam International in a diagonal and horizontal orientation with respect to the loading direction and underwent an AMS 5663 heat treatment. A group of specimens also underwent the HIP treatment. Samples were tested under stress controlled high cycle fatigue in stress amplitudes ranging from 200 MPa to 1200 MPa at a frequency of 50 Hz at both room temperature and 500°C. The machine used was a *Fatigue Dynamics RBF-200 HT* rotating beam tester. Specimens were cycled until

failure or a chosen endurance limit of 10^7 cycles. The results were compared with the data collected from a set of wrought Inconel 718 samples with the same heat treatment and available data on wrought Inconel 718 from literature.

Similarly to the data reported in literature, for each tested material, there is a decrease of the slope of the S-N curve at high temperature as compared to room temperature tests. The material has a longer life at 500°C for lower stress amplitudes than the material at room temperature. At higher stresses, the room temperature material outperforms material at 500°C. In general, the wrought material outperforms the DMLS diagonal material followed by the DMLS horizontal material at room temperature. At elevated temperature, the wrought and DMLS diagonal materials behave similarly and outperform the DMLS horizontal material followed by the DMLS HIPed material.

It can be concluded that high cycle fatigue performance is sensitive to the manufacturing technique and post-manufacturing treatments. In particular, the HIP treatment noticeably reduces the fatigue performance of the DMLS Inconel 718in the high cycle regime as seen in the low cycle regime.

Images were taken of select fracture surfaces of the tested Inconel 718 high cycle fatigue samples. There is a distinct pattern of brittle failure on the surface of the specimen and ductile failure in the center. The proportion of brittle fracture area to ductile fracture area varies with the material category. The DMLS HIPed material shows the largest area of brittle fracture, followed by the DMLS diagonal and horizontal material and wrought material. The proportion of brittle to ductile fracture area can be correlated to the fatigue performance of the materials, as the HIPed material performs notably worse than the DMLS diagonal and horizontal material and wrought material.

To study the low cycle fatigue behavior of a fiberglass reinforced vinylester composite, rectangular coupon specimens were manufactured by HALO Maritime Defense Systems according to ASTM D3039. Monotonic tension tests were first performed using a 250kN *MTS Landmark 270* servohydraulic testing system to compare to the manufacturer's reference data. The average ultimate tensile stress is 427.69 MPa with a 1.42% variation. The average tensile modulus is 22.91 GPa with a 7.94% variation. This is compared to the manufacturer's data of 12.4 GPa for tensile modulus and 137.9 MPa for the ultimate tensile strength. Even if a different criterion for failure is used (observation of micro-damage vs. macroscopic delamination) it still doesn't explain the lower value of the elastic modulus reported by the manufacturer. Overall, it appears that using the manufacturer's values of the tensile modulus and ultimate stress will constitute a conservative approach to design.

Tension-tension stress-controlled fatigue experiments were conducted for maximum stresses ranging from 250 MPa to 350 MPa usin a 250kN *MTS Landmark 270* servohydraulic testing system to investigate how the stress magnitude relates to the number of cycles to failure. The apparent stiffness of the material was monitored throughout the test, and failure was defined as a 0.5% change in the apparent stiffness over 5 cycles.

As expected, the number of cycles to failure decreases with increase in stress. For each experiment, there is some irreversible strain accumulated after the unloading in the first cycle due to the non-linear stress-strain response of the material. The major mode of failure in the material is delamination of the composite. For all samples tested, there is a sudden reduction in apparent stiffness at the failure point, although this reduction is insignificant during the life of the material. The apparent stiffness, therefore, is not a reliable property to monitor to accurately predict remaining life in the material. The high variability in cycles to failure for the same loading

amplitude seen in these tests, typical for composites, creates a large uncertainty in the material's life prediction. For this reason, a large batch of data should be collected and a lower bound S-N curve should be used for design purposes.

VII. REFERENCES

[1] E. C. Santos, M. Shiomi, K. Osakada, and T. Laoui, "Rapid manufacturing of metal components by laser forming," International Journal of Machine Tools and Manufacture, 46, 1459–1468, 2006.

[2] C. K. Chua and K. F. Leong, "Rapid Prototyping: Principles and Applications," 1. World Scientific, 2003.

[3] J. J. Beaman, J. W. Barlow, D. L. Bourell, R. H. Crawford, H. L. Marcus, and K. P. McAlea, "Solid Freeform Fabrication: A New Direction in Manufacturing," 2061. Kluwer Academic Publishers, 1997.

[4] L. Lü, J. Y. H. Fuh, and Y.-S. Wong, "Laser-Induced Materials and Processes for Rapid Prototyping." Kluwer Academic Publishers, 2001.

[5] G. N. Levy, R. Schindel, and J. P. Kruth, "Rapid Manufacturing and Rapid Tooling With Layer Manufacturing (Lm) Technologies, State of the Art and Future Perspectives," CIRP Annals - Manufacturing Technology, 52, 589–609, 2003.

[6] M. Greulich, "Rapid prototyping and fabrication of tools and metal parts by laser sintering of metal powders," Materials Technology, 12, 155–157, 1997.

[7] E. D. Herderick, "Progress in Additive Manufacturing," JOM, 67, 580–581, 2015.

[8] D. Cooper, J. Thornby, N. Blundell, R. Henrys, M. A. Williams, and G. Gibbons, "Design and manufacture of high performance hollow engine valves by Additive Layer Manufacturing," Materials and Design, 69, 44–55, 2015.

[9] X. Zhao, J. Chen, X. Lin, and W. Huang, "Study on microstructure and mechanical properties of laser rapid forming Inconel 718," Materials Science and Engineering A, 478, 119–124, 2008.

[10] K. N. Amato, S. M. Gaytan, L. E. Murr, E. Martinez, P. W. Shindo, J. Hernandez, S. Collins, and F. Medina, "Microstructures and mechanical behavior of Inconel 718 fabricated by selective laser melting," Acta Materialia, 60, 2229–2239, 2012.

[11] F. Liu, X. Lin, C. Huang, M. Song, G. Yang, J. Chen, and W. Huang, "The effect of laser scanning path on microstructures and mechanical properties of laser solid formed nickel-base superalloy Inconel 718," Journal of Alloys and Compounds, 509, 4505–4509, 2011.

[12] A. Simchi and H. Pohl, "Effects of laser sintering processing parameters on the microstructure and densification of iron powder," Materials Science and Engineering A, 359, 119–128, 2003.

[13] A. Riemer, S. Leuders, M. Thöne, H. A. Richard, T. Tröster, and T. Niendorf, "On the fatigue crack growth behavior in 316L stainless steel manufactured by selective laser

melting," Engineering Fracture Mechanics, 120, 15–25, 2014.

[14] T. R. Pollock and S. Tin, "Nickel based superalloys for advanced turbine engines: chemistry, microstructure and properties," Journal of propulsion and power, 22, 361–374, 2006.

[15] L. L. Parimi, G. Ravi, D. Clark, and M. M. Attallah, "Microstructural and texture development in direct laser fabricated IN718," Materials Characterization, 89, 102–111, 2014.

[16] E. Yasa and J. P. Kruth, "Microstructural investigation of selective laser melting 316L stainless steel parts exposed to laser re-melting," Procedia Engineering, 19, 389–395, 2011.

[17] S.-H. Chang, S.-C. Lee, T.-P. Tang, and H.-H. Ho, "Influences of Soaking Time in Hot Isostatic Pressing on Strength of Inconel 718 Superalloy," Materials Transactions, 47, 426–432, 2006.

[18] S.-C. Lee, S.-H. Chang, T.-P. Tang, H.-H. Ho, and J.-K. Chen, "Improvement in the Microstructure and Tensile Properties of Inconel 718 Superalloy by HIP Treatment," Materials Transactions, 47, 2877–2881, 2006.

[19] D. H. Smith, J. Bicknell, L. Jorgensen, B. M. Patterson, N. L. Cordes, I. Tsukrov, and M. Knezevic, "Microstructure and mechanical behavior of direct metal laser sintered Inconel alloy 718," Materials Characterization, 113, 1–9, 2016.

[20] L. Xiao, M. C. Chaturvedi, and D. L. Chen, "Low-cycle fatigue behavior of INCONEL 718 superalloy with different concentrations of boron at room temperature," Metallurgical and Materials Transactions A, 36, 2671–2684, 2005.

[21] R. T. Holt and W. Wallace, "Impurities and trace elements in nickel-base superalloys," International Metals Reviews, 21, 1–24, 1976.

[22] N. Kawagoishi, Q. Chen, and H. Nisitani, "Fatigue strength of Inconel 718 at elevated temperatures," Fatigue & Fracture of Engineering Materials & Structures, 209–216, 2000.

[23] S. Selvaraju and S. Ilaiyavel, "Applications of composites in marine industry," Journal of Engineering Research and Studies, 89–91, 2011.

[24] H. N. Narasimha Murthy, M. Sreejith, M. Krishna, S. C. Sharma, and T. S. Sheshadri, "Seawater Durability of Epoxy/Vinyl Ester Reinforced with Glass/Carbon Composites," Journal of Reinforced Plastics and Composites, 29, 1491–1499, 2009.

[25] David Miller; John F. Mandell; Daniel D. Samborsky; Bernadette A. Hernandez-Sanchez; D. Todd Griffith, "Performance of Composite Materials Subjected to Salt Water Environments," 2012 AIAA SDM Wind Energy Session, 2012.

[26] S. Gribbin, J. Bicknell, L. Jorgensen, I. Tsukrov, and M. Knezevic, "Low cycle fatigue behavior of direct metal laser sintered Inconel alloy 718," International Journal of Fatigue,

93, 156–167, 2016.

[27] E. Chlebus, K. Gruber, B. Kuźnicka, J. Kurzac, and T. Kurzynowski, “Effect of heat treatment on microstructure and mechanical properties of Inconel 718 processed by selective laser melting,” Materials Science and Engineering: A, 639, 647–655, 2015.

[28] F. Liu, X. Lin, G. Yang, M. Song, J. Chen, and W. Huang, “Microstructure and residual stress of laser rapid formed Inconel 718 nickel-base superalloy,” Optics and Laser Technology, 43, 208–213, 2011.

[29] G. A. Rao, M. Kumar, M. Srinivas, and D. S. Sarma, “Effect of standard heat treatment on the microstructure and mechanical properties of hot isostatically pressed superalloy inconel 718,” Materials Science and Engineering A, 355, 114–125, 2003.

[30] C. Wang and R. Li, “Effect of double aging treatment on structure in Inconel 718 alloy,” Journal of Materials Science, 39, 2593–2595, 2004.

[31] K. Sano, N. Oono, S. Ukai, S. Hayashi, T. Inoue, S. Yamashita, and T. Yoshitake, “γ″-Ni3Nb precipitate in Fe-Ni base alloy,” Journal of Nuclear Materials, 442, 389–393, 2013.

[32] M. G. Burke and M. K. Miller, “Precipitation in alloy 718: A combined Al3M and APFIM investigation,” Superalloys 718, 625 and Various Derivatives, 337–350, 1991.

[33] S. Ghosh, S. Yadav, and G. Das, “Study of standard heat treatment on mechanical properties of Inconel 718 using ball indentation technique,” Materials Letters, 62, 2619–2622, 2008.

[34] S. Azadian, L. Y. Wei, and R. Warren, “Delta phase precipitation in inconel 718,” Materials Characterization, 53, 7–16, 2004.

[35] J. R. Davis, “ASM Specialty Handbook: Heat-Resistant Materials,” in *ASM Specialty Handbook: Heat-Resistant Materials*, ASM International, 1997, 36.

[36] A. Chamanfar, L. Sarrat, M. Jahazi, M. Asadi, A. Weck, and A. K. Koul, “Microstructural characteristics of forged and heat treated Inconel-718 disks,” Materials and Design, 52, 791–800, 2013.

[37] C. A. Stein, A. Cerrone, T. Ozturk, S. Lee, P. Kenesei, H. Tucker, R. Pokharel, J. Lind, C. Hefferan, R. M. Suter, A. R. Ingraffea, and A. D. Rollett, “Fatigue crack initiation, slip localization and twin boundaries in a nickel-based superalloy,” Current Opinion in Solid State and Materials Science, 18, 244–252, 2014.

[38] ASTM International, “E606 / E606M-12: Standard Test Method for Strain-Controlled Fatigue Testing,” 2012.

[39] Y. C. Chiou and M. C. Yip, “Effect of mean strain level on the cyclic stress-strain behavior of AISI 316 stainless steel,” Materials Science and Engineering A, 354, 270–278, 2003.

[40] G. Salerno, R. Magnabosco, and C. Mouraneto, “Mean strain influence in low cycle fatigue

behavior of AA7175-T1 aluminum alloy," International Journal of Fatigue, 29, 829–835, 2007.

[41] Y. Gong and M. P. Norton, "Strain-Controlled Cumulative Fatigue with Mean Strains and High- Cycle and Low-Cycle Interaction," Journal of Testing and Evaluation, 25, 429–438, 1997.

[42] S. D. Antolovich, "Microstructural aspects of fatigue in Ni-base superalloys," Philosophical Transactions of the Royal Society A: Mathematical, Physical and Engineering Sciences, 373, 1–36, 2015.

[43] D. D. Krueger, S. D. Antolovich, and R. H. Van Stone, "Effects of grain size and precipitate size on the fatigue crack growth behavior of alloy 718 at 427 °C," Metallurgical Transactions A, 18, 1431–1449, 1987.

[44] H. Mecking and U. F. Kocks, "Kinetics of flow and strain-hardening," Acta Metallurgica et Materialia, 29, 1865–1875, 1981.

[45] M. Knezevic, J. S. Carpenter, M. L. Lovato, and R. J. McCabe, "Deformation behavior of the cobalt-based superalloy Haynes 25: Experimental characterization and crystal plasticity modeling," Acta Materialia, 63, 162–168, 2014.

[46] M. Zecevic, R. J. McCabe, and M. Knezevic, "Spectral database solutions to elasto-viscoplasticity within finite elements: Application to a cobalt-based FCC superalloy," International Journal of Plasticity, 70, 151–165, 2015.

[47] M. Knezevic, M. Zecevic, I. J. Beyerlein, J. F. Bingert, and R. J. McCabe, "Strain rate and temperature effects on the selection of primary and secondary slip and twinning systems in HCP Zr," Acta Materialia, 88, 55–73, 2015.

[48] N. E. Dowling, "Mechanical behavior of materials : engineering methods for deformation, fracture, and fatigue." Boston: Pearson, 2013.

[49] O. H. Basquin, "The exponential law of endurance tests," Proceedings of the American Society for Testing and Materials, 625–630, 1910.

[50] L. F. Coffin Jr., "A study of the effects of cyclic thermal stresses on a ductile metal," Transactions of the ASME, 76, 931–950, 1954.

[51] P. P. Gillis, "Manson-Coffin fatigue," Acta Metallurgica, 14, 1673–1676, 1966.

[52] Systems Integrators L.L.C., "RBF-200 HT Owners Manual." Systems Integrators L.L.C., Glendale, 2011.

[53] B. R. Plastics, "Structural Products: PROForms and PROPlate." 2014.

[54] ASTM International, "D3039/D3039M-14: Standard test method for tensile properties of polymer matrix composite materials," 2014.

[55] ASTM International, “D3479/D3479M-12: Standard Test Method for Tension-Tension Fatigue of Polymer Matrix Composite Materials,” 2012.

[56] C. E. Demers, “Tension–tension axial fatigue of E-glass fiber-reinforced polymeric composites: fatigue life diagram,” Construction and Building Materials, 12, 303–310, 1998.

[57] ASTM International, “E739-10: Standard Practice for Statistical Analysis of Linear or Linearized Stress-Life and Strain-Life Fatigue Data,” Annual Book of ASTM Standards, 2015.

[58] V. M. Harik, J. R. Klinger, and T. A. Bogetti, “Low Cycle Fatigue of Unidirectional Laminates : Stress Ratio Effects,” Journal of Engineering Materials and Technology, 122, 415–419, 2000.